Technical Evaluation of DC-DC Converter Output Filter

Marika Honka

School of Electrical Engineering

Thesis submitted for examination for the degree of Master of Science in Technology.

Espoo 20.4.2020

Thesis supervisor:

Prof. Jorma Kyyrä

Thesis advisor:

M.Sc. Mikko Taulanne

Aalto University
School of Electrical
Engineering

AALTO UNIVERSITY
SCHOOL OF ELECTRICAL ENGINEERING

ABSTRACT OF THE
MASTER'S THESIS

Author: Marika Honka

Title: Technical Evaluation of DC-DC Converter Output Filter

Date: 20.4.2020 Language: English Number of pages: 9+61

Department of Electrical Engineering and Automation

Professorship: Power Electronics

Supervisor: Prof. Jorma Kyyrä

Advisor: M.Sc. Mikko Taulanne

DC-DC converters play a vital role in a wide range of industrial applications, including fuel cells, marine vessels, and photovoltaic systems. A subset of DC-DC converters is bi-directional DC-DC converters, which allow the power to flow from the common DC bus to the energy storage and vice versa. In order to achieve high energy efficiency and extend the lifetime of the energy storage, it is necessary to minimize the output current and voltage ripple of the converter. In addition to this, a small filter size is preferred to improve cost-effectiveness.

This thesis studies different solutions for the output filter of the bi-directional interleaved three-phase DC-DC converter. The objective is to find the most cost-effective design with improved power density. In this thesis, three filter designs are presented and compared: LC, LCL, and the coupled-inductor. Filters are dimensioned to maintain the same output current ripple level and reduce the size and cost of the design compared to a reference L filter of 360 μH. AC equivalent circuit analysis is performed to determine sufficient component values for the filters. The performance of the dimensioned filter options is verified through simulation.

The LC filter is found to be the most cost-effective solution for the output filter of the bi-directional interleaved DC-DC converter. By adding a DC film capacitor to the filter circuit, the filter inductance can be reduced by 50 %, which leads to significant material reduction. However, the solution increases both the current stress of the semiconductors and the overall losses of the system.

Keywords: Bi-directional DC-DC converter, coupled inductor, LC filter, LCL filter, inductance

AALTO-YLIOPISTO
SÄHKÖTEKNIIKAN KORKEAKOULU

DIPLOMITYÖN
TIIVISTELMÄ

Tekijä: Marika Honka

Työn nimi: Tasasähkökatkojan lähtösuodattimen tekninen arviointi

Päivämäärä: 20.4.2020 Kieli: Englanti Sivumäärä: 9+61

Sähkötekniikan ja automaation laitos

Professuuri: Tehoelektroniikka

Työn valvoja: Prof. Jorma Kyyrä

Työn ohjaaja: DI Mikko Taulanne

Tasasähkökatkojalla on useita tärkeitä käyttökohteita teollisuudessa mukaan lukien polttokennot, laivojen sähköjärjestelmät ja aurinkosähköjärjestelmät. Kaksisuuntaiset tasasähkökatkojat ovat tasasähkökatkojien alakategoria, joka mahdollistaa tehon siirtymisen DC-kiskoilta energiavarastoon ja päinvastoin. Tasasähkökatkojan lähtövirran ja -jännitteen sykkeisyyden pienentäminen on tärkeää järjestelmän energiatehokkuuden parantamiseksi ja energiavaraston eliniän pidentämiseksi.

Tämä työ tutkii erilaisia vaihtoehtoja kaksisuuntaisen kolmivaiheisen tasasähkökatkojan lähtösuodattimelle. Työn tavoite on löytää kustannustehokkain ja järjestelmän tehotiheyttä parantava vaihtoehto. Työssä esitellään kolme eri suodatinratkaisua: LC, LCL ja kytketty kuristin. Suodatinratkaisujen mitoituksen lähtökohta on ylläpitää sama lähtövirran sykkeisyys ja pienentää suodattimen kokoa ja materiaalikustannuksia verrattuna 360 μH L-suodattimeen. Suodatinratkaisujen komponenttiarvot määritettiin sijaiskytkentäpiirien AC-analyysillä ja suorituskyky varmistettiin piirisimuloinneilla.

Työssä LC-suodatin osoittautui kustannustehokkaimmaksi suodatinratkaisuksi kaksisuuntaiselle tasasähkökatkojalle. Suodattimen induktanssia voidaan pienentää jopa 50 % lisäämällä suodatinpiiriin filmikondensaattori. Pienempi induktanssiarvo vähentää myös suodattimen materiaalikustannuksia. Suodatinratkaisu kuitenkin lisää puolijohteiden virtarasitusta ja kasvattaa koko järjestelmän häviöitä.

Avainsanat: Kaksisuuntainen tasasähkökatkoja, kytketty kuristin, LC-suodatin, LCL-suodatin, induktanssi

Preface

This master thesis was commissioned by the System Drives department of ABB Oy. I want to thank all my colleagues at ABB Oy for their support during the writing of this thesis and my career.

I want to thank my advisor Mikko Taulanne for his valuable advice and support during the process. Special thanks to Lauri Peltonen and Joonas Puukko for their advice and guidance for this thesis. I also want to thank my supervisor Jorma Kyyrä for all professional comments and corrections to the thesis.

I express my gratitude to all my friends and family for their support. Warmest gratitudes to HTMK16 and Radiodiodi for all the memorable moments during my years of university studies. Last but not least, I want to show my deepest gratitude to my significant other Jan Tuomi for his love and encouragement during my studies and this thesis.

Otaniemi, 20.4.2020

Marika Honka

Contents

Symbols and abbreviations

Symbols

a	Steinmetz coefficient for determining core loss
A_c	Cross-sectional area of the magnetic core
B, $\mathbf{B}$	Magnetic flux density
$\hat{B}_{ac}$	Peak value of the flux density
B_{max}	Maximum allowed flux density
B_{p2p}	Peak-to-peak flux density
B_r	Remanence flux density
B_{sat}	Saturation flux density
C	Capacitance
C_f	Filter capacitance
D	Duty cycle
$\mathbf{E}$	Electric field intensity
E_{Batt}	Electromotive force of a battery
E_n	Sinusoidal voltage source
E_{rr}	Reverse recovery energy of a diode
E_{sw}	Rated switching loss energy per pulse
f	Frequency
f_0	Resonance frequency
f_{sw}	Switching frequency
H, $\mathbf{H}$	Magnetic field intensity
H_c	Coercivity field intensity
H_e	Effective magnetic field intensity
i	Instantaneous current
i_c	Capacitor current
i_{cond}	Semiconductor current during the conduction period
i_L	Inductor current
$i_{L,peak}$	Peak value of the inductor current
i_o	Output current
$i_{o,p2p}$	Output current ripple
$I_{c,p2p}$	Average output current ripple of coupled-inductor
I_C	Collector current
I_{DC}	DC current
I_L	Average inductor current
$I_{L,crit}$	Critical inductor current
$I_{n,p2p}$	Average phase current ripple
$I_{nc,p2p}$	Average output current ripple of non-coupled inductor
I_{nom}	Reference commutation voltage of a semiconductor
I_o	Average output current
I_p	Peak current
j	Harmonic number
J, $\mathbf{J}$	Electrical current density

k	Steinmetz coefficient for determining core loss
k_e	Eddy-current loss coefficient
k_i	Material parameter of iGSE
l	Total length of the magnetic path
l_c	Mean length of the magnetic core
l_g	Total air gap length
L	(Self-)inductance
L_{eq}	Equivalent inductance
L_f	Filter inductance
L_{lk}	Leakage inductance
L_{min}	Minimum filter inductance
L_{nc}	Inductance of the non-coupled inductor
L_{ss}	Steady-state inductance
L_{tr}	Transient inductance
m_L	Total mass of the inductor
M	Mutual inductance
n	Number of phases
n_s	Effective phase count
N	Number of turns
P_c	Core loss
P_{cond}	Average conduction loss
P_{ec}	Eddy-current loss
P_c	Core loss per unit volume
P_{sw}	Switching loss of a semiconductor
P_w	Winding loss
R_{Batt}	Equivalent series resistance of a battery
$\Re$	Magnetic reluctance
$\Re_g$	Reluctance of the air gap
$\Re_c$	Reluctance of the core
s	Laplace variable
S, $\mathbf{S}$	Enclosed surface
t	Time
T_c	Curie-temperature
T_{core}	Core temperature
T_{sw}	Switching period
T_w	Winding temperature
u	Instantaneous voltage
u_{cond}	Semiconductor voltage during the conduction period
u_L	Inductor voltage
U	Average voltage
U_{CE}	IGBT collector-emitter voltage
U_{DC}	DC input voltage
U_{ES}	Energy storage voltage
U_{GE}	IGBT gate-emitter voltage
$U_{GE(th)}$	IGBT threshold voltage

U_{in}	Average input voltage
U_{nom}	Reference commutation voltage of a semiconductor
U_o	Average output voltage
V_c	Volume of the magnetic core
W_c	Core loss per one hysteresis cycle
x_{yoke}	Inductor core length
y_{yoke}	Inductor core width
z_{tot}	Total height of the filter inductor
Z_{tot}	Total impedance
α	Coupling coefficient
β	Steinmetz coefficient for determining core loss
Δ	Variable change
ϵ	Permittivity of the medium
μ	Magnetic permeability
μ_0	Permeability of the free space, $4\pi \times 10^{-7}$ [H/m]
μ_e	Effective permeability
μ_r	Relative permeability of the material
ρ	Electrical resistivity
τ	Turn-on period of a semiconductor
Φ	Magnetic flux
Φ_c	Magnetic flux in the core
Φ_g	Magnetic flux in the air gap

Abbreviations

AC	Alternating current
CCM	Continuous-conduction mode
DC	Direct current
DDC	Bi-directional interleaved three-phase DC-DC converter
DCM	Discontinuous-conduction mode
DV	Design variable
EMI	Electromagnetic interference
ES	Energy storage
ESR	Equivalent series resistance
FOM	Figure of merit
IGBT	Insulated-gate bipolar transistor
MMF	Magnetomotive force
PFC	Power-factor correction
PQ	Power quality
PWM	Pulse-width modulation
RM	Rectangular modular
SE	Steinmetz Equation
iGSE	improved Generalized Steinmetz Equation

1 Introduction

DC-DC converters play an important role in a wide range of industrial applications, such as fuel cells, marine vessels, and photovoltaic systems. In addition to these, DC-DC converters are an essential building block in systems that handle conversions between AC and DC voltages. [1] There are multiple different DC-DC converter topologies, all of which can be categorized as transformer-isolated or non-isolated, as well as unidirectional or bi-directional.

This thesis studies a bi-directional interleaved three-phase DC-DC converter (DDC) focusing on the output filter design. In a DDC, energy can be transferred through the power unit in both directions between the common DC bus and the energy storage (ES). For example batteries, supercapacitors, and fuel cells can work as energy storage. The energy storage allows for several benefits compared to a system without one. Compensating peak power demand, smoothing power variations in the system, and providing back-up power in case of a blackout are just a few examples.

Energy efficiency, reliability, high power density, and cost-efficiency are critical features of an economically feasible power electronic system [1]. As such, it is necessary to minimize the current and voltage ripple of the ES in order to reduce the internal losses and achieve high energy efficiency [2]. Increased current ripple leads to higher temperatures of the ES, which may shorten the lifetime of the system [3]. Even though the output current ripple of the DDC is significantly reduced by virtue of an interleaved control method, additional filtering of unwanted high-frequency components is required.

The objective of this thesis is to find the most cost-effective output filter design for DDC with improved power density. Important design parameters for the filter include output current ripple, efficiency, size, and cost. The thesis presents three different output filter designs: LC, LCL, and the coupled-inductor. With higher-order filter topologies, such as LC and LCL, it is possible to reduce the size of individual components. In turn, a coupled-inductor reduces the current stress of semi-conductor switches while maintaining the same output current ripple. The resulting filter designs are compared to a reference inductor design of 360 μH.

The thesis is divided into chapters as follows. Chapter 2 discusses the basics of switch-mode DC-DC converters including, step-up and step-down topologies, operation modes of the converter, interleaved bi-directional DC-DC converter, and losses in DC-DC converters. Chapter 3 presents the fundamentals of electromagnetism and the theory behind the design of inductive components. Chapter 4 discusses the solution alternatives for the output filter of the DDC. Chapter 5 presents the dimensioning of the three previously mentioned filter designs and the simulation models to verify the calculated results. Equivalent circuit analysis is performed for each solution to determine sufficient component values. Based on the calculations and simulation results, three example filter inductor designs are introduced and compared. Finally, the conclusion of the study is presented in Chapter 6.

2 DC-DC converter

Many industrial applications, such as fuel cells, photovoltaic systems and energy storage, require DC voltages, and currents to be converted to a specific level. A DC-DC converter is an electric power converter that uses high-frequency switching to regulate voltage levels. The output DC voltage level can be modified by adjusting the duty cycle D. [1]

A bi-directional interleaved three-phase DC-DC converter (DDC) is a type of converter in which the power can flow in or out of the converter. When the power flows towards the load, the converter works like a Buck converter. Equivalently, when the power is transferred from the load to the converter, the device operates as a Boost converter. The structure and operation of the DDC are further discussed in Chapter 2.3.

This chapter focuses on the operation of the bi-directional switch-mode DC-DC converter as well as the Buck and Boost converters incorporated in its topology. The converters are analyzed in steady state and in periodic operation with switching frequency f_{sw}. The semiconductor switches and passive components (L and C) are considered ideal, and as such, the losses of these components are neglected, and the switching is immediate.

2.1 Buck and Boost converter

A Buck converter is presented in Figure 1. This type of converter is also called a step-down converter since the average output voltage U_o is always lower than the average input voltage U_{in}. In the converter, a power transistor and a diode operate as a bi-positional switch, which can be either on or off. When the switch is on, the transistor is conducting, and a positive voltage is applied across the inductor, $u_L = U_{in} - U_o$. This causes the inductor current i_L to increase linearly. After the transistor is switched off, the inductor current continues to flow through the diode. However, since the voltage across the inductor is now negative, the inductor voltage equals $u_L = -U_o$, which causes the inductor current i_L to decrease and the magnetic energy in the inductor to be transferred to the load. [4]

In steady state, the average voltage across the inductor over the switching cycle is

$$\frac{1}{T_{sw}} \int_0^{T_{sw}} u_L dt = 0 \tag{1}$$

Equation (1) implies that the areas A and B from Figure 2 must be equal. Therefore,

$$(U_{in} - U_o)D = U_o(1 - D) \tag{2}$$

from which

$$D = \frac{U_o}{U_{in}} \tag{3}$$

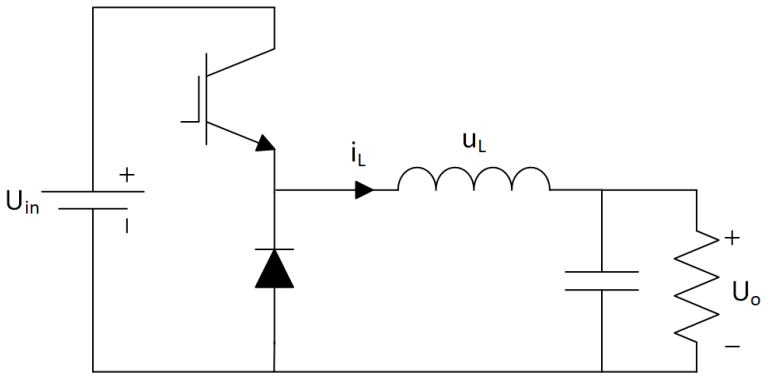

Figure 1: Buck converter.

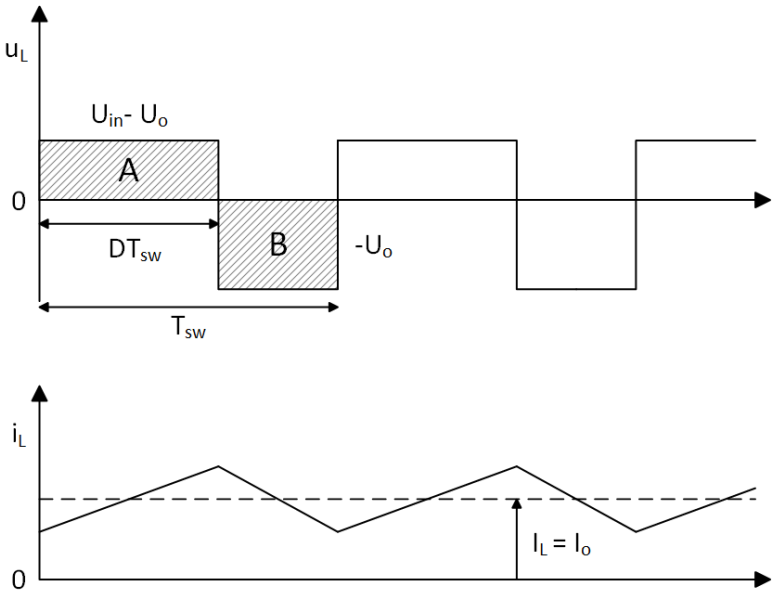

Figure 2: Currents and voltages of the Buck converter during one operation cycle.

A Boost converter is also called a step-up converter, since the average output voltage U_o is higher than the input voltage U_{in}. The structure of a Boost converter is shown in Figure 3. Similar to a Buck converter, there is a bi-positional switch which consists of a power transistor and a diode. When the transistor is conducting, the input

voltage U_{in} is applied across the inductor which causes the inductor current i_L to increase linearly as seen in Figure 4. When the transistor is turned off and the diode becomes forward biased, the current flows to the load. During the switching cycle, energy is stored in and released from the inductor while i_L increases and decreases respectively. [4]

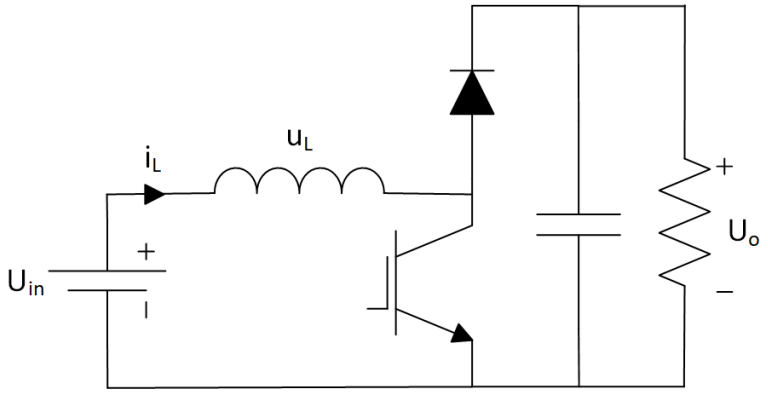

Figure 3: Boost converter.

Again, Equation (1) indicates that the areas A and B must be equal. Therefore,

$$U_{in}D = (U_o - U_{in})(1 - D) \tag{4}$$

from which

$$\frac{U_o}{U_{in}} = \frac{1}{1 - D} \tag{5}$$

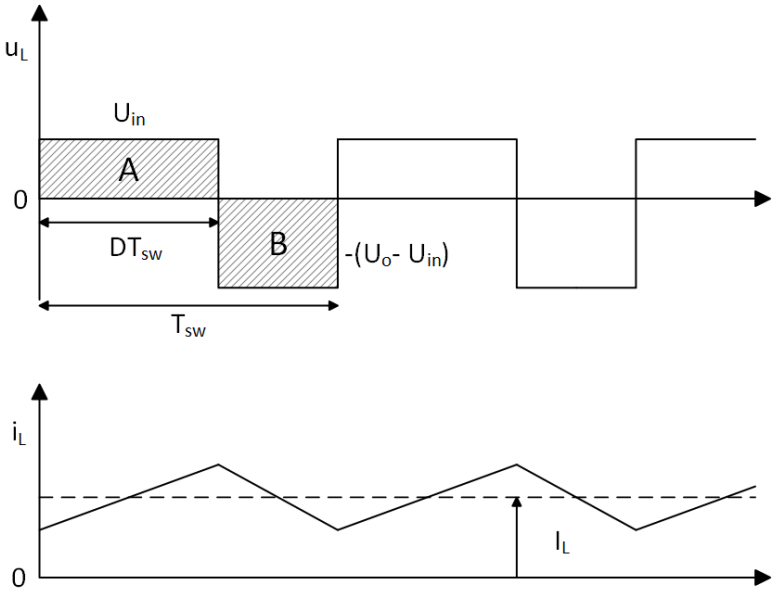

Figure 4: Currents and voltages of the Boost converter during one operation cycle.

These analyses hold only in the continuous-conduction mode (CCM) when the inductor current flows continuously, i.e. $i_L > 0$. If i_L reaches zero, the converter enters discontinuous-conduction mode DCM. There is no current flow in the circuit until the beginning of the next switching cycle since the current direction cannot reverse. Recognizing the correct operation mode of the converter is crucial since the derived equations for duty cycle are not valid in DCM. [5]

2.2 Discontinuous Conduction Mode (DCM)

Due to their structure, unidirectional DC-DC converters have two operation modes: continuous-conduction and discontinuous conduction mode. When the output load decreases while the duty cycle D remains unchanged, the average inductor current I_L decreases until the instantaneous inductor current i_L reaches zero at the end of the switching cycle. This average inductor current is known as critical inductor current $I_{L,crit}$. Since in unidirectional DC-DC converters the power and current flow cannot reverse, the converter enters discontinuous conduction mode (DCM) below the critical inductor current $I_{L,crit}$, and the inductor current remains zero until the beginning of the next switching cycle. [1]

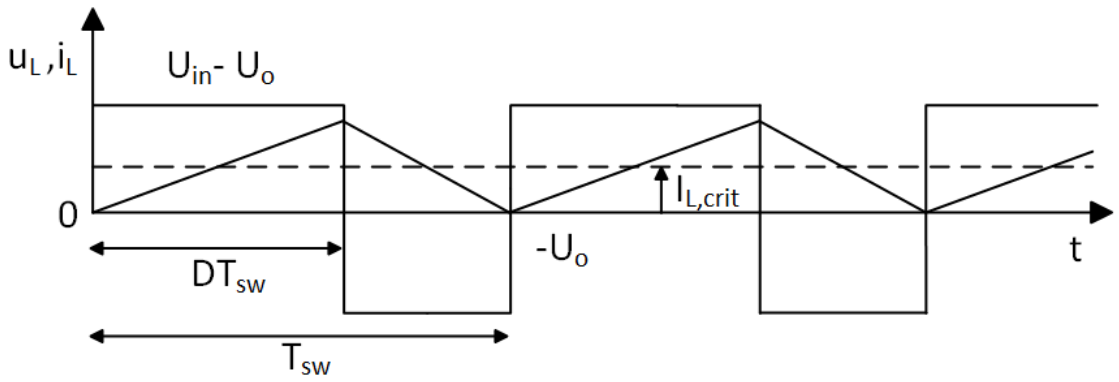

Figure 5: The critical current of a Buck converter.

Figure 5 shows the critical inductor current of a Buck converter. As seen from the figure, the critical inductor current $I_{L,crit}$ is half the inductor current peak value $i_{L,peak}$. From this definition, the critical inductor current can be calculated for Buck and Boost converters as follows.

For the Buck converter:

$$I_{L,crit} = \frac{1}{2} i_{L,peak} = \frac{DT_{sw}}{2L}(U_{in} - U_o) \tag{6}$$

For the Boost converter:

$$I_{L,crit} = \frac{1}{2} i_{L,peak} = \frac{U_o T_{sw}}{2L} D(1 - D) \tag{7}$$

In DCM, the interval of inactivity increases device stresses and ratings of the passive components. In addition to this, the operation mode results in more EMI and noise. Thus, DC-DC converters with a power range above a few tens of watts are designed to operate mainly in CCM. [1] This thesis assumes continuous-conduction mode in all calculations and simulations. The inductance of the converter circuit is dimensioned so that the converter operates in CCM at nominal output current.

2.3 Interleaved bi-directional DC-DC converter

Multiphase DC-DC converters are widely used in power electronic applications due to their several advantages over their single-phase counterparts. Single-phase DC-DC converters have some limitations in high-current applications related to large current ripple and high power loss in the filter inductor. Multiphase DC-DC converters reduce the current and voltage stress of the semiconductor switches. Also, step-up and step-down converters are not applicable for bi-directional power transmission. [6][7]

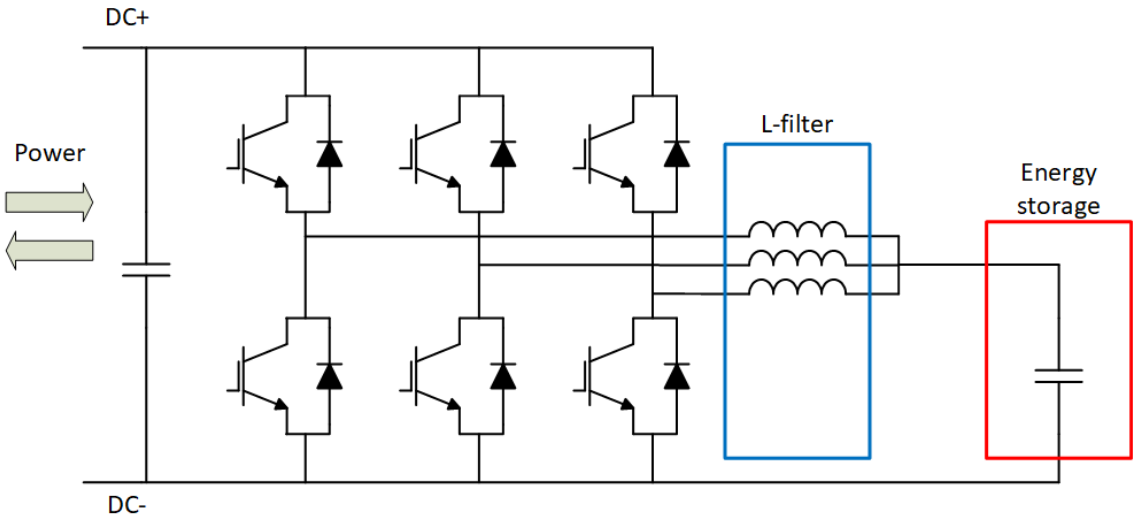

Figure 6: Bi-directional DC-DC converter.

Figure 6 shows the structure of a bi-directional three-phase DC-DC converter. The converter consists of six switches, two for each converter leg. An IGBT and an antiparallel connected diode form one bi-positional switch. The structure is the same for a two-level inverter which allows versatile use of the power module. Here, the converter structure serves as three parallel-connected Buck or Boost converters, depending on the direction of the power flow. [6]

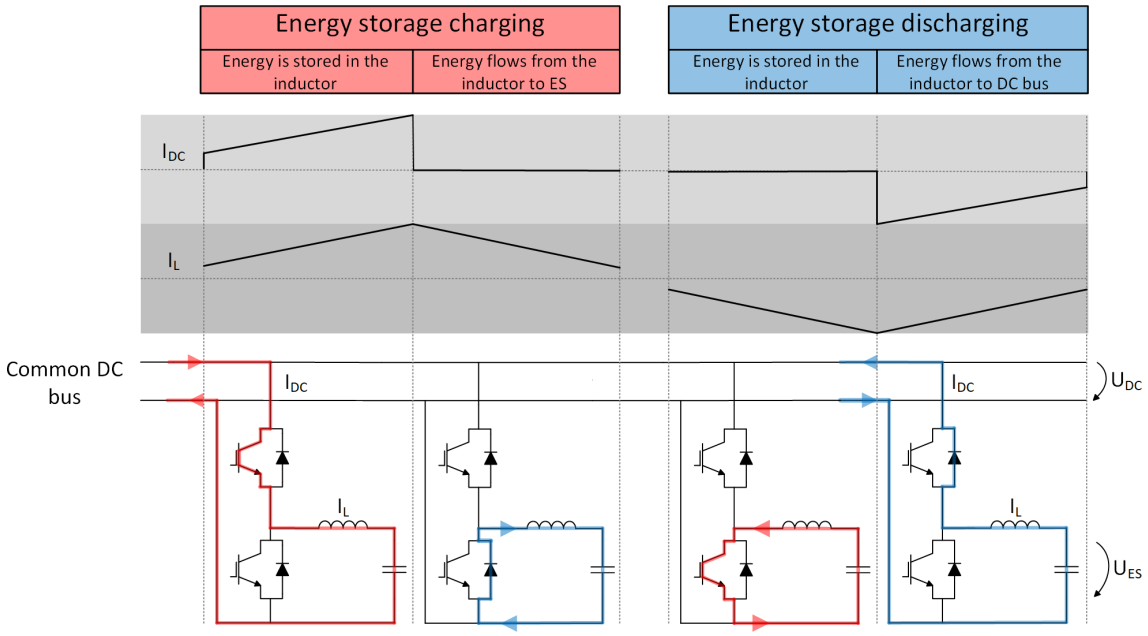

Figure 7: Buck and Boost mode operation of a bi-directional interleaved DC-DC converter.

Figure 7 describes both operation modes of the DDC. In Buck mode, only the upper IGBT and the lower diode of each converter leg are conducting alternatingly. When the IGBT is switched on, the diode becomes reverse-biased, and the inductor current increases linearly. After switching off the IGBT, the current continues to flow through the diode, since the current direction cannot change abruptly. Respectively, in Boost mode, only the lower IGBT and upper diode are conducting.

In the interleaved multiphase DC-DC converter, each phase-leg is controlled independently of the other two legs. Control waveforms are similar to those for single-phase DC-DC converter, except that each leg is phase-shifted by T_{sw}/n. [1] The output current of the interleaved converter I_o is the sum of the phase currents. The output current ripple of n-phase interleaved converter for given switching frequency, duty cycle and inductance can be calculated as follows

$$i_{o,p2p} = n_s \frac{DU_{DC}(1-D)}{Lf_{sw}} \tag{8}$$

$$n_s = \frac{\left(D - \frac{\lfloor n \cdot D \rfloor}{n}\right) \cdot \left(\frac{1 + \lfloor n \cdot D \rfloor}{n} - D\right)}{D(1-D)} \tag{9}$$

where n_s is the effective phase count. With interleaved modulation and appropriate phase shift among the parallel switches, the ripple components of both the input

and output current are greatly reduced since switching ripples cancel each other. Figure 8 shows the output and phase currents of a three-phase interleaved DC-DC converter. The maximum current ripple is divided by the number of interleaved phases and the frequency of the ripple is $n \cdot f_{sw}$. Lower current ripple reduces the size of the passive components and allows the use of a lower switching frequency. Lower switching frequency also reduces the switching losses of the semiconductors. [3][8]

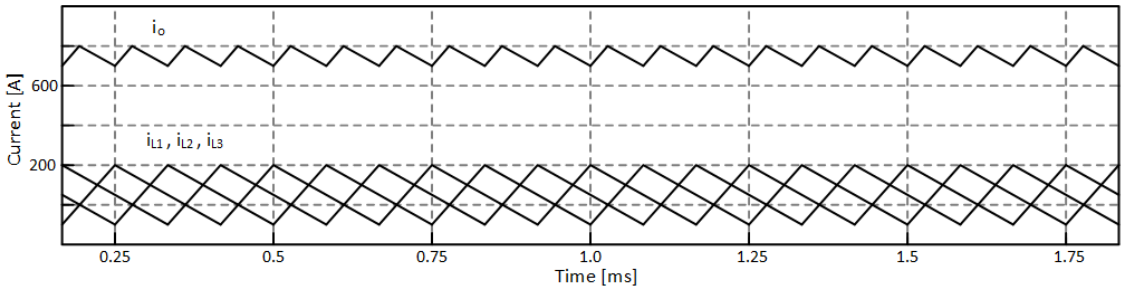

Figure 8: Output and phase currents of a three-phase interleaved DC-DC converter.

2.4 Losses in DC-DC converters

In switch-mode power converters, the semiconductor devices must be able to control the power flow to the load with minimum power dissipation. High power dissipation in the semiconductors increases the junction temperature and could lead to degradation in electrical characteristics and thermal runaway. Therefore, losses of semiconductor devices are an essential design criterion that affects cooling and energy efficiency of a converter. Primarily, the losses of the module occur in semiconductor devices. At power levels of few MWs and switching frequencies below a few tens of kHz, an IGBT is the most commonly used switching component in switch-mode power converters. [1][9] This chapter describes the switching characteristics and the power dissipation of the IGBT.

Figure 9 presents the current and voltage waveforms for the turn-on and turn-off for the IGBT. First, the current flows through the upper diode in Figure 9. At t_0, the lower IGBT is turned on by a positive gate drive voltage. The gate-emitter voltage U_{GE} rises, and at t_1, it exceeds the threshold voltage $U_{GE(th)}$. The current through IGBT increases as the current through the diode decreases. The reverse current of the diode generates a peak in the collector current waveform. Between t_2 and t_3, the collector-emitter voltage decreases quickly as the voltage over the diode increases; making the diode current sharply decrease. Once the reverse recovery time is over, the gate-emitter voltage remains constant due to the Miller-capacitance until the collector-emitter voltage reaches zero at t_4. After this, the gate-emitter voltage increases to the value of the gate drive voltage. [10]

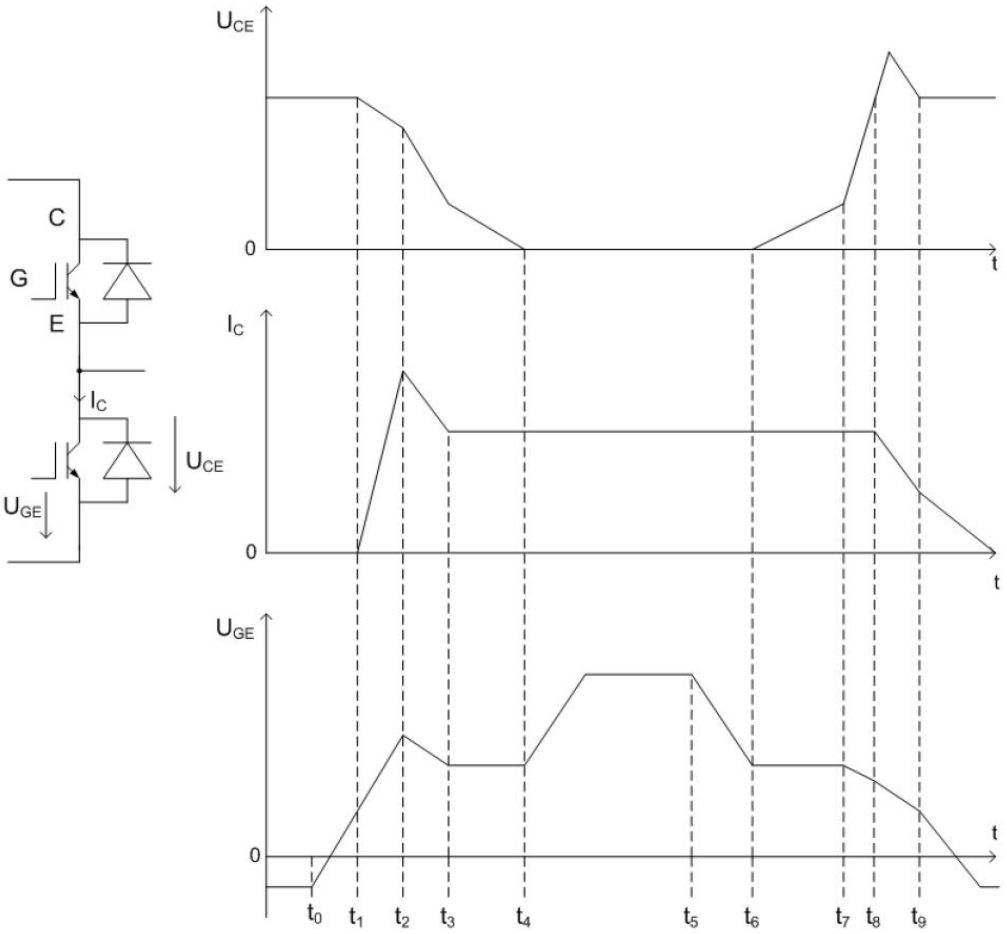

Figure 9: IGBT current and voltage waveforms during the turn-on and turn-off. [11]

The turn-off of the IGBT involves the events that occurred during the turn-on in the reversed order. At t_5, the gate input voltage changes to blocking state value, which causes the gate-emitter voltage to decrease. Shortly after this, the collector-emitter voltage begins to rise. Between t_6 and t_7, the Miller effect momentarily prevents the decrease of the gate-emitter voltage. At t_8, the U_{GE} is dropped below the level required to sustain the current flow, which results in the rapid decrease of the collector current. The "tailing" current continues to flow even after the collector-emitter voltage has stabilized. The IGBT is not switched off until the collector current is zero. [10]

Losses of the semi-conductor switches consist of conduction losses and switching losses. During turn-on and turn-off, power loss occurs primarily during the crossover time when both voltage and current are relatively high. The average conduction loss over the switching cycle for the diode or IGBT is

$$P_{cond} = \frac{1}{T_{sw}} \int_0^{\tau} u_{cond}(t) \cdot i_{cond}(t) \cdot dt \tag{10}$$

where T_{sw} is the switching period, u_{cond} is the voltage over the component, i.e. DC input voltage, i_{cond} is the current through the component, i.e. inductor current, and τ is the turn-on period. [12]

This thesis assumes a linear loss model for semi-conductor switching, i.e., switching losses are linear with respect to the current and voltage. Switching losses for IGBT and diode are linearized according to Equation (11)

$$P_{sw} = f_{sw} E_{sw} \frac{i}{I_{nom}} \frac{U_{DC}}{U_{nom}} \tag{11}$$

where f_{sw} is the switching frequency, E_{sw} is the rated switching loss energy per pulse for given reference commutation current I_{nom} and voltage U_{nom}, i is the instantaneous value of the current, and U_{DC} is the DC input voltage. For diode, the losses due to reverse recovery energy are calculated using the same equation, the switching energy of Equation (11) is changed to reverse recovery energy of the diode E_{rr}. [12][13]

As seen from Equations (10) and (11), losses of the IGBT are directly proportional to the switching frequency. At higher switching frequencies, the switching losses dominate over the conduction loss. Thus, increased semiconductor losses and limited cooling capacity restrict the switching frequency of the DDC. [4]

3 Magnetic theory

Magnetic components, such as inductors and transformers, are widely used in power electronics. This chapter discusses the theory behind inductor design, including the fundamentals of electromagnetism and magnetic components. The chapter presents different inductor core shapes and materials as well as outlines hysteresis and losses in magnetic materials.

3.1 Electromagnetic laws

Maxwell's laws together with Lenz's law form a basis for magnetic theory and are useful when designing transformers and inductors. A conductor carrying electrical current induces a magnetic field around the conductor. The direction of the magnetic field intensity H is determined by a thumb-rule. According to the rule, if a conductor is held in right hand, the thumb shows the direction of the current while the other fingers indicate the direction of the magnetic field. [14] According to Ampère's law, the integral of H around a closed path equals the current flowing through the enclosed surface:

$$\oint_l \boldsymbol{H} \cdot d\boldsymbol{l} = \int_S \boldsymbol{J} \cdot d\boldsymbol{S} + \frac{\partial}{\partial t} \int_S \varepsilon \boldsymbol{E} \cdot d\boldsymbol{S} \tag{12}$$

Here the latter term, also referred as displacement current, is neglected. In power electronics, the current density J is assumed to have a magnitude of 10^6 A/m^2 and the second term, or displacement current, is assumed to be no more than 10 A/m^2. [14] Both sides of the equation represent a phenomenon called magnetomotive force (MMF). If the MMF is produced by a current carrying coil with N turns, Equation (12) simplifies to form:

$$\oint_l \boldsymbol{H} \cdot d\boldsymbol{l} = \int_S \boldsymbol{J} \cdot d\boldsymbol{S} = Ni \tag{13}$$

A time-changing flux $\Phi(t)$ through a closed path induces a voltage to the loop. The sign of the voltage is opposite to the rate of change of the flux. Faraday's law describes this relation between the generated voltage and the time-changing flux as

$$\oint_l \boldsymbol{E} \cdot d\boldsymbol{l} = -\frac{d}{dt} \int_S \boldsymbol{B} \cdot d\boldsymbol{S} \tag{14}$$

where

$$\Phi = \int_S \boldsymbol{B} \cdot d\boldsymbol{S} \tag{15}$$

Φ is the magnetic flux passing through a surface. Magnetic field density from Faraday's law and magnetic flux density from Ampère's law are linked to each other. [14] This connection is called magnetic permeability μ

$$\boldsymbol{B} = \mu \boldsymbol{H} = \mu_r \mu_0 \boldsymbol{H} \tag{16}$$

Gauss's law for magnetics circuits states that a total flux through a any closed surface S is zero. Therefore, the total flux entering the the volume is always equal to the flux coming out of the volume, i.e. magnetic monopoles do not exist. It is analogous to the Kirchoff's current density law. [14]

$$\oint_S \boldsymbol{B} \cdot d\boldsymbol{S} = 0 \tag{17}$$

3.2 Magnetic circuits

Inductors can be used to filter high-frequency components, limit rapid current changes and store energy in the magnetic field [10]. In this thesis, the inductors are mainly used for filtering high-frequency components from the output current. Furthermore, the operation of a DC-DC converter requires a large enough inductor for temporary energy storage. Inductance characterizes the tendency of an electrical conductor to oppose the change in electric current flowing though the component. By definition, inductance is the derivative of the flux linkage:

$$L = N\frac{d\Phi}{di} \tag{18}$$

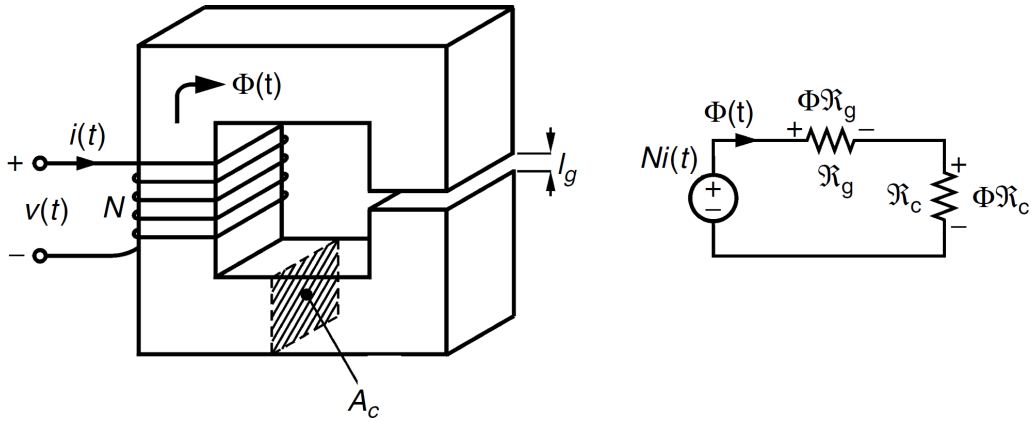

Figure 10: Magnetic circuit with and air gap, both physical structure and equivalent circuit. [14]

According to Faraday's law (14), a changing current flowing through an inductive component induces a voltage opposite to the rate of change. Therefore, a voltage over an ideal inductor is:

$$u_L = L\frac{di}{dt} \tag{19}$$

Figure 10 shows a simple magnetic circuit with an air gap. A coil with N turns carrying AC current produces MMF in the circuit and magnetic flux Φ flows through

the core. The relation between the magnetomotive force and the magnetic flux is called reluctance $\Re$. Reluctance of the magnetic material characterizes the core resistance to the magnetic flux flow and is analogous to electric resistance. The equivalent circuit of the magnetic structure is shown in Figure 10. The magnetic field intensity H is assumed to be uniform in both parts, i.e. fringing flux is neglected. This assumption is valid only for small air gaps. According to Ampère's law

$$Hl_c + Hl_g = Ni \tag{20}$$

Applying Gauss's law (17) to the equivalent circuit:

$$\Phi_c + \Phi_g = 0 \tag{21}$$

Equation (20) can be written as:

$$\Phi(\Re_c + \Re_g) = Hl_c + Hl_g \tag{22}$$

where

$$\Re = \frac{l}{\mu A_c} \tag{23}$$

The reluctance is directly proportional to the length of the magnetic path and inversely proportional to the cross-sectional area of the core A_c. Furthermore, magnetic reluctance depends on the permeability of the material. In magnetic circuits, reluctances can be connected in series or in parallel like resistances in electric circuits. However, magnetic reluctance is an energy storing element and not an energy consuming one. [14][15]

3.3 Core materials

Important properties from the design point of view are saturation B_s, permeability μ, resistivity ρ, coercivity H_c and remanence B_r. Materials can be divided into three groups depending on their magnetic properties: diamagnetic, paramagnetic and ferromagnetic. For diamagnetic and paramagnetic materials, the relative permeability is near unity. Paramagnetic materials are slightly magnetized when exposed to a magnetic field. For diamagnetic materials, the relative permeability is slightly less than unity, and therefore, they exclude magnetic fields. Ferromagnetic materials are the most important group of core materials when designing magnetic components for power electronics. Their relative permeability μ_r is on a magnitude of 10 to 100 000. However, when ferromagnetic material is heated above its Curie-temperature T_c, the permeability of the material drops to 1 and both coercivity and remanence become zero. [14]

Ferromagnetic materials consist of microscopic magnetized domains in the crystals of the material. These are called Weiss domains. Without the influence of an external magnetic field, they are randomly aligned resulting in zero net field in the material. Figure 11 shows the B-H curve of the ferromagnetic material. In the beginning, the magnetic field intensity H and the magnetic flux density B are both zero.

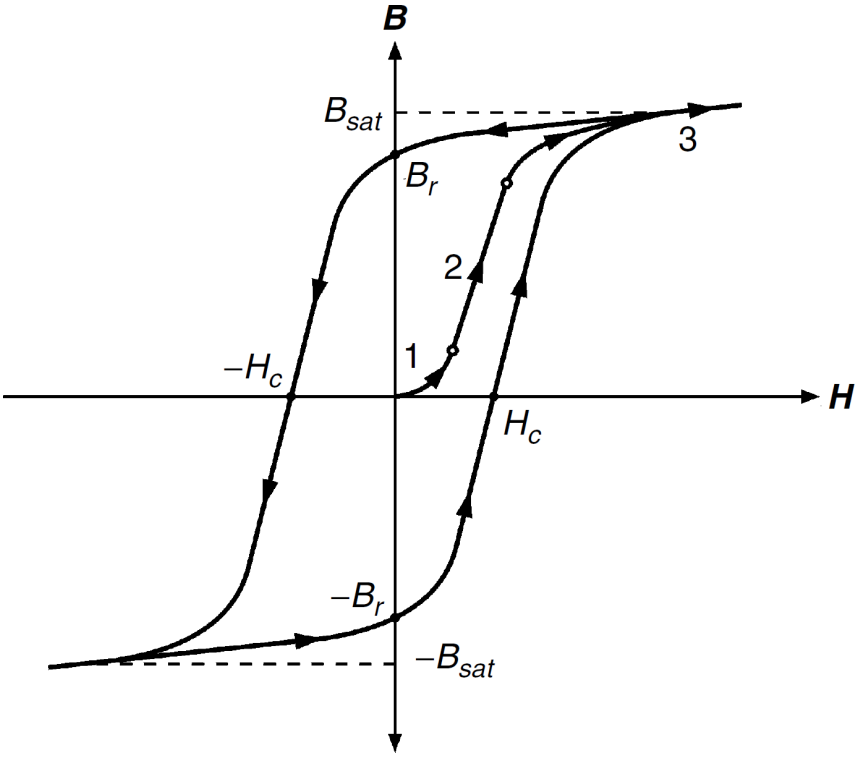

Figure 11: Hysteresis loop and magnetization curve. [14]

First, when magnetic field intensity H increases, the flux density B also increases along the numbered curve. The first section of the curve corresponds to reversible Weiss domain wall displacements. In the second section of the curve, the domains are subjected to a torque in the external field aligning them with the direction of the field. When nearly all domains are aligned with the external field, further increase in field intensity H does not result significant increase in flux density B. The magnetic flux density has reached a saturation point B_{sat} in the third section of the curve. When the external field is removed, the magnetic flux density also decreases but remains non-zero. This value is called the remanence flux density B_r. A reverse external magnetic field needs to be applied to reduce the remanence flux density to zero. The field intensity value at which flux density reduces to zero, is called coercivity of the material H_c. If field intensity H further increases to the opposite direction, the material is magnetized as described above and the magnetic flux density reaches the saturation point. If H cycles between the maximum values, the curve traces out the hysteresis loop shown in Figure 11. The area inside the hysteresis loop equals the losses during one cycle. In the process of magnetization and demagnetization the magnetic flux density lags behind the magnetic field intensity. This phenomenon is known as hysteresis. [14][15]

Ferromagnetic materials can be further divided into soft and hard magnetic materials. Soft magnetic materials are easy to magnetize and demagnetize. The coercivity force H_c is low and the hysteresis loop is narrow, as seen in Figure 12. Most magnetic

components in power electronics are made from soft magnetic materials. In hard magnetic materials, also known as permanent magnets, the coercivity force H_c is high and the material resists the external magnetic force. Permanent magnets produce magnetic flux without an external field, thus making the remanence flux B_r high. Compared to the soft magnetic materials, the hysteresis loop is wide and resembles a square, as shown in Figure 12. Generally, materials with $H_c < 1000$ A/m are classified as soft magnetic materials while materials with $H_c > 10\ 000$ A/m are classified as hard magnetic materials. [14]

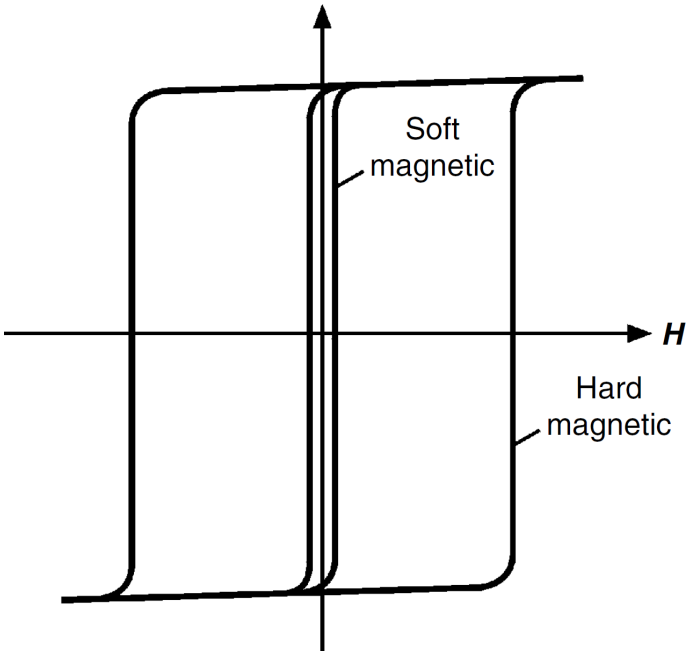

Figure 12: Hysteresis loop of soft and hard magnetic materials. [14]

Desirable properties for an inductor material are low coercivity H_c and losses, as well as high relative permeability μ_r, resistivity ρ, and saturation flux B_{sat}. Mainly two types of materials are used in power electronic applications: ferromagnetic materials and ferrites. Ferromagnetic materials are iron alloys which also contain some amounts of chrome (Cr), cobalt (Co), nickel (Ni) and silicon (Si). Ferrites are ceramic materials of iron oxides (Fe_2O_4) mixed with manganese (Mn), zinc (Zn), cobalt and nickel. Ferrites have high resistivity ρ, but they are fragile and hard to process. Advantages of ferrites include low losses even in higher frequencies (3 MHz). As for ferromagnetic materials, they have low resistivity ρ, high B_{sat} and μ_r. [14]

Soft ferromagnetic material cores are made out of thin laminated stacks due to their high electrical conductivity. Insulation layers between the metal sheets reduce eddy-current losses. Iron is often alloyed with other elements for different applications. Higher relative permeability is achieved by alloying iron with nickel whereas higher saturation magnetic flux density B_{sat} is attained by alloying cobalt with iron. Silicon steel is widely used in low frequency magnetic applications. Adding silicon to iron reduces the resistivity of the material, and thus, eddy-current losses in the core. It

also increases relative permeability of the alloy, reducing the hysteresis losses of the core. Other advantages include reduction of acoustic noise due to reduction of magnetostriction. However, silicon content decreases the saturation flux density B_{sat} and Curie temperature T_c. Usually, silicon content is no more than 3% due to mechanical processing difficulties above that level and avoiding brittle structure. [14][16]

Anisotropic magnetic properties further reduce the hysteresis loss in laminated cores. Since the magnetic flux passes in the direction of the laminations in laminated cores, it is beneficial to increase the permeability of the material in this direction and reduce it in the direction perpendicular to the lamination plane. In the grain-oriented silicon steel, the permeability is higher in the rolling direction, hence reducing the hysteresis loss and temperature rise in laminated cores. [14]

Powdered iron is manufactured from iron with low carbon content by grinding it into small particles. Particles are electrically isolated from each other by coating them with insulating material. As a result, powdered iron cores can store considerable amount of energy in the non-magnetic binding material between the particles. The core inherently provides an evenly distributed air gap in the structure, which lowers the relative permeability. Powdered iron cores attain a high saturation flux density $B_{sat} = 1.3$ T, and have relatively high resistivity ρ and low eddy-current loss. [16]

Carbonyl iron cores are manufactured by heating carbonyl iron $Fe(CO)_5$. The structure is microspherical and onionlike. The alloy contains 0.8 % carbon which affects to hysteresis loss negatively. Therefore, carbon content is often reduced further. The material has relatively low permeability, between 1 and 50. However, the permeability is almost constant in contrast to magnetic field and frequency. Other advantages include high saturation flux density $B_{sat} = 1.9$ T and temperature stability ranging from -55° to + 150 °C. The losses per volume are higher than in the ferrite core at the same induction level. Both powdered iron and carbonyl iron are easy to process without special tools. The tolerance of the dimensions is lower compared to the ferrite cores. [14]

Ferrites are chemically inert, hard and brittle metallic oxides. They are favored material especially in high frequency applications because of their high resistivity. In high frequencies the eddy-current losses are dominant. These are inversely proportional to the resistivity of the material. Most commonly used ferrimagnetic alloys are manganese-zinc (MnZn) and nickel-zinc (NiZn). MnZn ferrites have a high relative permeability μ_r and high saturation flux density B_{sat}. NiZn ferrites are characterized by a high resistivity up to 10^7 Ω·m, relatively low Curie temperature, $T_c = 150 - 300°$ C and low saturation flux density B_{sat}. They are also difficult to process and susceptible to mechanical stress such as vibration and high rate cooling. [16]

Amorphous materials are alloys of iron and magnetic or other transition metals. The atomic structure of amorphous materials differs greatly from crystalline metals, since it is similar to that of glass or liquids. The material is often referred as metallic glass. The chemical, magnetic and mechanical properties of amorphous material are different from those of crystalline metal alloys. The material is manufactured by rapidly quenching hot molten metal by compressing it on a cooling roller. Rapid cooling prevents the formation of the crystalline structure. B_{sat} varies from 0.7 T to 1.8 T. The material has a linear hysteresis loop and high permeability. A thin 10-50 μm ribbon has low resistivity which leads to low eddy-current losses. The Curie-temperature of the material is 350-450 °C. Losses in amorphous materials are nearly independent of temperature changes and some materials even have a negative temperature coefficient. [14]

Nanocrystalline materials are the newest magnetic material used in power electronic applications. Nanocrystalline materials consist of ultrafine crystals, typically having a size of 7-20 nm. These materials combine high saturation magnetic flux density B_{sat} of silicon steel and low high-frequency losses of the ferrites. The initial permeability is in the range of 15 000 to 150 000 and the Curie temperature of the material is approximately 600 °C. However, nanocrystalline cores are very brittle and often need to have extra protection, like epoxy coating or a plastic core box, against mechanical stress. [14]

3.4 Inductor structure

The structure of an inductor is similar to the transformer. However, the purpose of these components is different; it is beneficial for an inductor to store energy in the magnetic field , unlike a transformer, for which this is not a desirable feature. Adding an air gap to the core permits much higher levels of magnetic flux density and thus increases the amount of energy stored in the inductor, compared to the core without an air gap. Adding an air gap to the core increases the overall reluctance of the magnetic component. A core with an air gap requires a larger current to achieve the same magnetic flux as a core without an air gap. As a consequence, air gaps are usually added to the inductor core to avoid saturation. [16][17]

Effect of the air gap on the magnetization curve is shown in Figure 13. The slope of the curve equals the effective permeability of the of the magnetic component. As seen from Figure 13, the air gap increases the linear part of the *B-H* curve. Without an air gap, the magnetic flux is only limited by the material properties, making the slope as steep as possible. Adding an air gap to the core results in a more stable and predictable inductance at the expense of the overall inductance value. Increasing the air gap can lead to additional EMI at higher frequencies and increased winding losses. [15][16]

Magnetic cores are made in various shapes and sizes for different applications and power ratings. Such shapes include toroids, pot cores, power quality (PQ) cores, rectangular modular (RM) cores, CC cores, UU cores, UI cores, EE cores, and EI cores. These core shapes are used in the design of inductors and transformers.

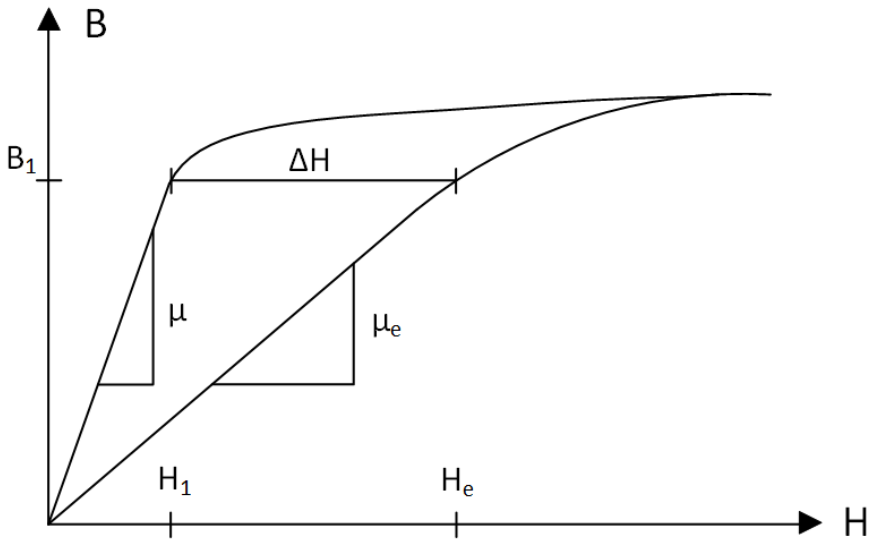

Figure 13: The effect of the air gap in the magnetization curve. Without an air gap, the field intensity corresponding to magnetic field density B_1 is H_1. Adding an air gap to the core increases the corresponding field intensity value to H_e, flattening the B-H curve.

Figure 14 a) shows a few common core shapes with windings. The windings can be wound on a bobbin made of dielectric material. [16]

The choice of core geometry affects winding losses, production costs, and leakage flux, which is defined as the magnetic flux outside the inductor. Leakage flux increases the total magnetic flux in the core, which may lead to saturation of the core. [16]

There is almost no leakage flux in toroidal cores since the magnetic field is constrained by the core material. Windings of the toroidal inductors are more expensive than in bobbin wound inductors since the wire must be wound through the hole of the core. [16]

In pot cores, the coil is wound on a bobbin and enclosed in core material. The majority of the magnetic flux is in the interior of the core, leading to reduced leakage flux. However, heat removal from the winding and the core to the outer surface is restricted and may cause temperature to rise greatly in high-current applications. The RM core is similar to the pot core except for sections cut off on both sides of the skirt. Wider openings assist in heat removal and allow for the usage of thicker wires. [16]

Core shapes in Figure 14 b) and their variations are suitable for high power applications. E cores are the most widely used core shapes because of their low cost and availability in large sizes. The coil can be wound using conventional winding

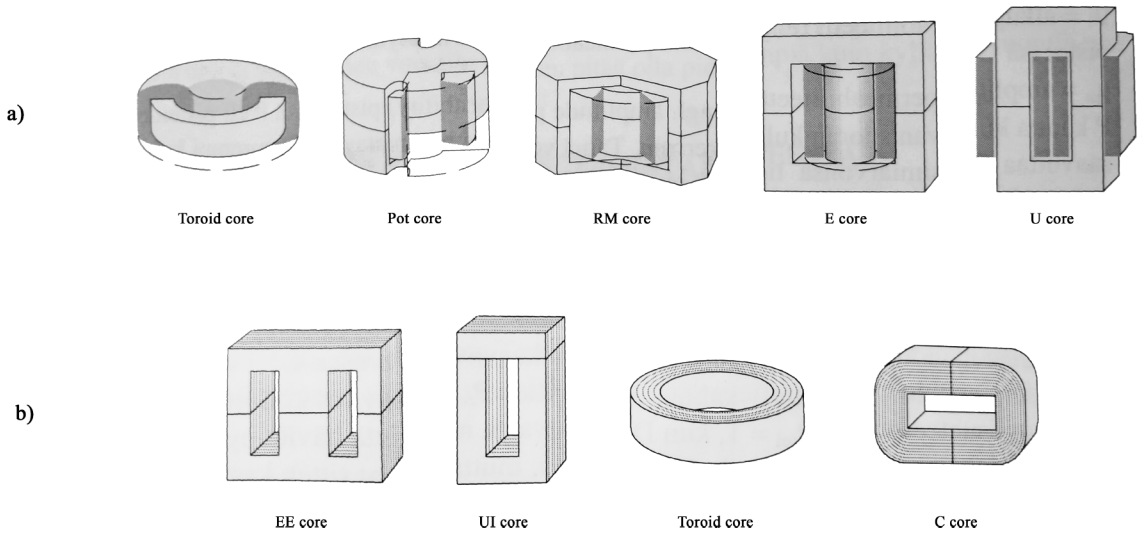

Figure 14: Different core shapes of inductive components. a) Five common core shapes and their windings and b) core shapes used in sheet, wound and powdered cores. [18]

machines, hence lowering the production cost. A round center leg in E cores shortens the winding mean turn length by 11 % compared to the square center leg which reduces the magnet wire cost and weight, winding resistance, and winding losses. In E and U cores, the windings are not completely surrounded by magnetic material which increases the leakage flux. However, the more open structure allows for increased airflow, which reduces the temperature. [16] E and U shapes are combined with an I-part or another matching E- or U-part. EE and UI are typical shapes for laminated cores whereas CC is a typical shape for wound cores. [18]

3.5 Losses in magnetic components

Losses of the inductor can be categorized roughly to winding losses and magnetic core losses. Winding losses can be further divided into AC losses and DC losses. DC loss can be expressed with DC resistance of the coil which can be calculated using the cross sectional area of the wire, average turn length and resistivity of the winding material. In low frequencies, DC resistance describes the winding losses quite accurately. [18]

When calculating AC resistance, both proximity effect and skin-effect need to be taken into account. These phenomena result in nonuniform current density J, and thus, increase losses in the conductor. A time-varying high frequency current induces a magnetic field in the conductor. The skin effect is caused when the conductor is affected by its own magnetic field which induces eddy-currents to the wire. This causes the current density to decrease towards the center of the wire, i.e. the current

tends to flow at the surface of the wire. The proximity effect is also a result of eddy-currents. The conductor is subjected to the magnetic field of adjacent conductors or winding layers which induce eddy-currents to the wire. Magnetic fields of adjacent conductors may add or subtract depending on the current direction. The proximity effect is a major loss mechanism in high-frequency inductors and transformers. Due to these two phenomena, the effective resistance of the conductor and the power loss increase as the frequency increases. At low frequencies, the current takes the path of the lowest resistance, but when the frequency increases, the current takes the path of the lowest inductance. [16][18]

The air gap of the core increases winding losses. The magnetic flux lines do not travel straight across the air gap. Instead, the flux lines bulge outward as the magnetic lines repel each other in the nonmagnetic material. This effect called fringing is shown in Figure 15. The fringing flux is proportional to the length of the gap. The fringing flux induces eddy-currents in the winding when it penetrates the winding in transverse direction. This may even lead to overheating in the vicinity of the air gap. To prevent detrimental effects, long air gaps are divided into multiple smaller ones. The winding should be spaced at least two gap lengths away from the air gap by increasing the thickness of the bobbin. [16][18]

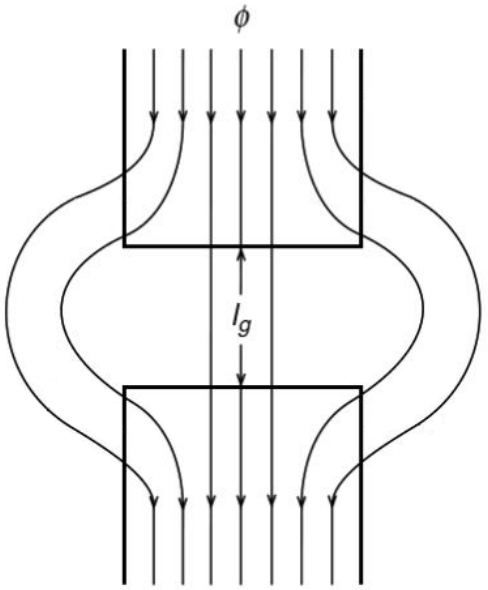

Figure 15: Fringing effect in the air gap of an inductor. [16]

Core losses of the inductor consist of eddy-current losses and hysteresis loss. Parameters affecting the core loss are the core geometry, material and thickness. When magnetizing and demagnetizing the magnetic core, the energy flowing from the source to the coil is greater than the energy returned to the source. The area of the

hysteresis loop is proportional to the core loss per one hysteresis cycle

$$W_c = V_c \oint \boldsymbol{H} \cdot d\boldsymbol{B} \tag{24}$$

where V_c is the volume of the magnetic core. The integral represents the energy loss density in the core. Core loss represents the energy used to align and rotate magnetic moments of the material. The core loss increases as the operating frequency and AC flux density increase. The general form of the core loss per unit volume is

$$P_c = k f^a (\hat{B}_{ac})^\beta \tag{25}$$

where coefficients k, a, and β are empirically determined and depend on the core material and frequency range, and $\hat{B}_{ac}$ is the peak value of the flux density of the applied field. This empirical equation is called the Steinmetz Equation (SE) and the parameters k, a and β are accordingly called Steinmetz parameters. However, SE is not always suitable for core loss calculation for several reasons. The equation is valid only for sinusoidal excitation and the parameters are valid only for specific flux density and frequency range. In addition to this, take equation does not take account the possible premagnetization of the material. For more accurate core loss calculation a variation of the improved Generalized Steinmetz Equation (iGSE) can be used.

$$P_c = k_i (2f)^a B_{p2p}^\beta \tag{26}$$

where k_i, a and β are empirically determined material parameters and B_{p2p} is the peak-to-peak flux density. [19]

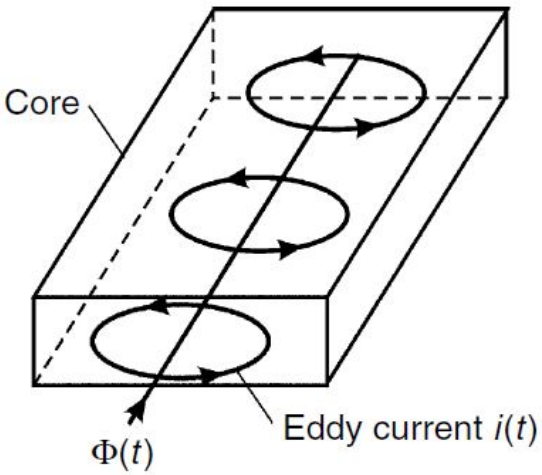

Figure 16: Eddy currents in the inductor core. [14]

According to Faraday's law, a time-varying flux induces a voltage in the core. Induced voltage generates circulating eddy-currents in the conducting core, as seen in Figure 16. Eddy-current losses in the core can be calculated with an equation similar to Equation (25).

$$P_{ec} = k_e \frac{f^2(\hat{B}_{ac})^2}{\rho} \tag{27}$$

where k_e is the eddy-current loss coefficient and ρ is the resistivity of the core material. Eddy-current losses are proportional to the induced voltage and inversely proportional to the internal resistivity of the core. Thus, using high-resistivity or laminated core material reduces the resistive eddy-current losses. [14][16]

4 Filters in power electronics

Filters in power electronic converters mainly consist of inductors and capacitors. In addition to these, some filter circuits, like snubbers and du/dt filters, include resistances. However, these filters are not examined in this thesis. Simply put, on the DC side, an inductor is smooths the output current, and a capacitor reduces voltage ripple. [20] Optimal design of higher-order filters requires careful selection of capacitance and inductance values. While higher-order filters consist of a greater number of components, the individual component values are lower.

4.1 Design constraints

An output filter inductance of a DC-DC converter has various requirements and design constraints related to converter operation and control. Important design parameters include output current ripple, efficiency, and size. Actual filter design is often a well-balanced compromise between different design parameters and overall cost [17].

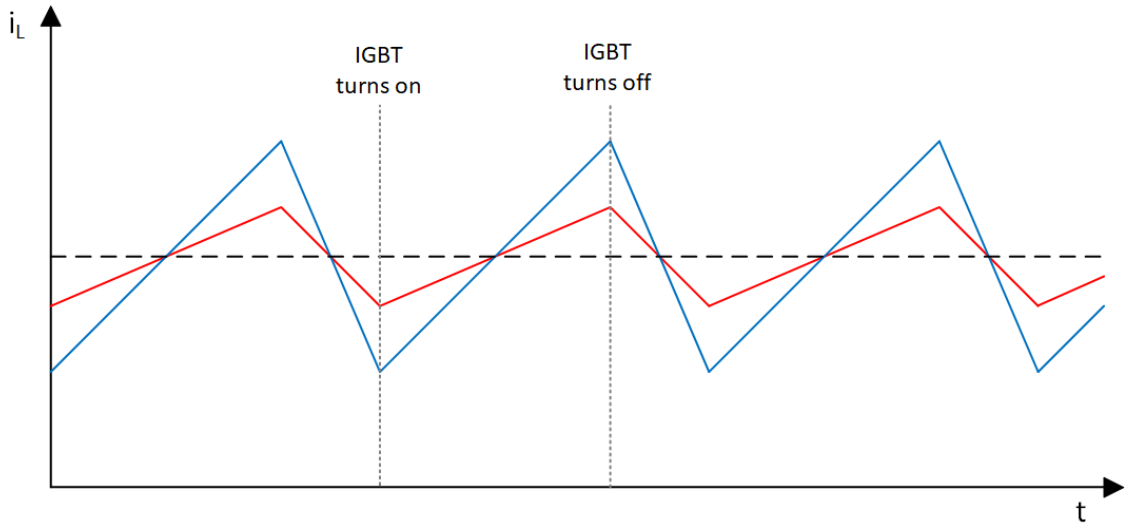

Figure 17: Two inductor currents with different peak-to-peak values. The average value of the currents is marked with dashed line. Decreasing filter inductance increases the current ripple.

For high-power converters, high efficiency is a vital requirement. Therefore, minimization of component losses is crucial. [20] Increasing filter inductance reduces the phase current ripple, and thus, conduction loss of the semiconductors. The effect on switching losses depends on the semiconductor device and, more precisely, the relation of the turn-on and turn-off energies of the semiconductor device. Figure 17 shows two inductor currents with the same frequency and average value, differing only in peak-to-peak value. It can be seen from the figure that as the peak-to-peak current increases, the turn-on current decreases correspondingly while the turn-off current

increases. Turn-on and turn-off energies vary depending on the semiconductor. For example, in the case of Infineon IGBT module FS500R17OE4DP, the turn-on energy is higher than the turn-off energy [21].

Filter inductance is often the bulkiest component of the DC-DC converter. The reduction of total inductance can lead to a significant reduction of both physical size and material costs. The smaller inductance value also improves the transient performance of the DC-DC converter. [22]

4.2 L and LC filter

High-frequency switching generates ripple in the output of the DC-DC converter. Passive filters consisting of inductors and capacitors are used in order to minimize the current and voltage ripple. Multiple different filter topologies exist. The simplest topology is called an L filter, which is a series inductor connected to the output of the converter. A single-phase connection of an L filter is highlighted with a dashed line in Figure 18. The Bode diagram of the L filter is shown in Figure 19. The diagram describes the behaviour of the L filter in the frequency domain. The L filter is a first-order filter with 20 dB attenuation per decade over the whole frequency range. The impedance of the L filter increases as the frequency increases, i.e., the attenuation of the signal is proportional to the frequency. Increasing switching frequency moves current ripple components to higher frequencies but also increases switching losses of the semiconductor switches. [23]

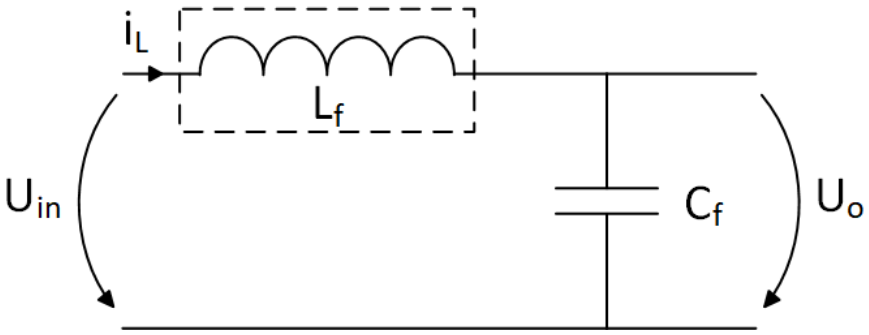

Figure 18: Single-phase connection of LC filter.

A single-phase connection of an LC filter is shown in Figure 18. A capacitor added in parallel with an inductor forms a second-order filter with resonance frequency f_0. As seen from the Bode diagram in Figure 20, the frequency range is divided in two at the resonance frequency. The filter has no gain on frequencies less than f_0. On frequencies greater than f_0, the filter provides 40 dB attenuation per decade. The LC filter should be designed so that none of the harmonic components of the signal are amplified by the gain surrounding the resonance frequency. The resonance frequency is also affected by the load impedance. A damping circuit can be added to suppress the gain at resonance frequency. However, an additional damping resistor is not preferable for

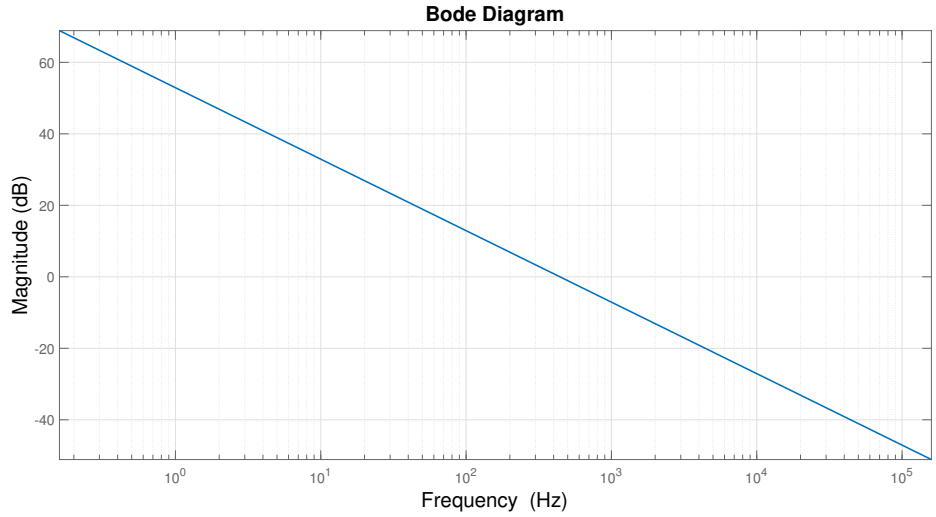

Figure 19: Bode diagram of an L filter with $L_f = 360$ μH.

power ratings greater than hundreds of kilowatts, since the power dissipation of the resistor becomes large. [20][23] The resonance frequency of the LC filter is calculated as:

$$f_0 = \frac{1}{2\pi}\frac{1}{\sqrt{LC}} \tag{28}$$

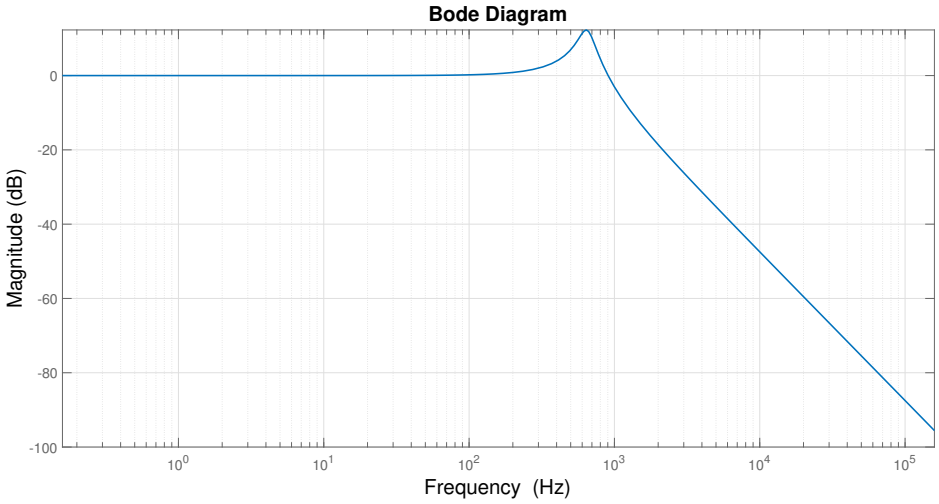

Figure 20: Bode diagram of an LC filter with $L_f = 60$ μH and $C_f = 1000$ μF.

4.3 LCL filter

LCL filters are widely used for AC-side filtering in grid connected inverters. A single-phase connection of an LCL filter is shown in Figure 21. In AC-side filtering, the LCL topology is preferred over LC since the additional inductor improves the decoupling between the filter and the grid impedance, thus reducing the dependence of the grid parameters. Also compared to an LC filter, the current stress over the grid side inductor is smaller. [23]

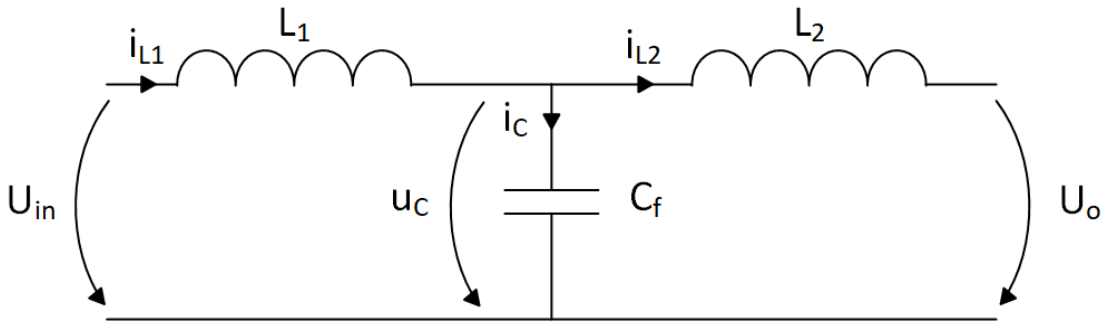

Figure 21: Single-phase connection of an LCL filter.

Figure 22 shows the Bode diagram of an LCL filter. The attenuation of the LCL filter is 60 dB per decade at frequencies above the resonance frequency. The high level of attenuation allows for lower switching frequency and inductance values. The total inductance of an LCL filter can be made much smaller than in simple L filters [24]. However, the LCL filter greatly magnifies frequencies near the resonance frequency and is vulnerable to oscillations. While damping circuits can be added to minimize the negative effects of the resonance frequency, resonance frequency is still an important design parameter. [23]

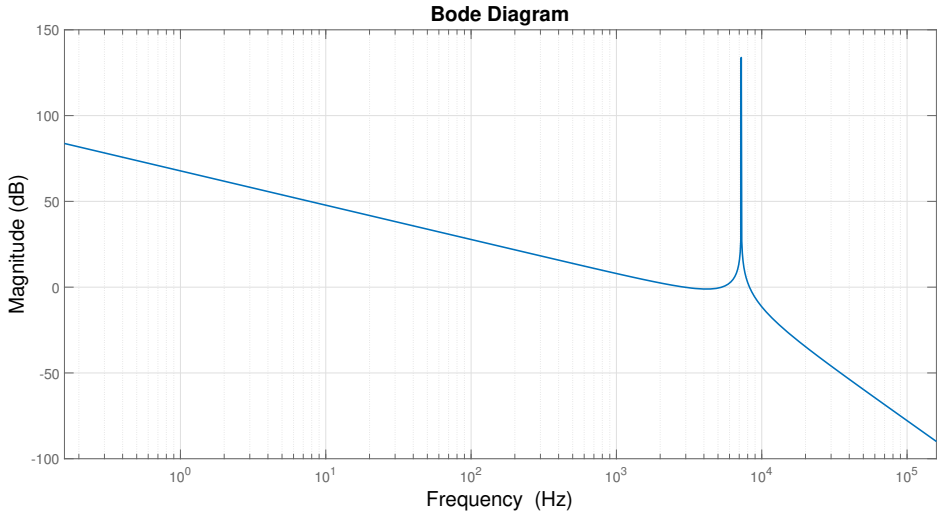

Figure 22: Bode diagram of LCL filter $L_1 = 60$ μH, $C_f = 105$ μF, and $L_2 = 5$ μH.

When designing an LCL filter for the AC side, the resonance frequency of the filter should be at minimum ten times of the fundamental frequency and at maximum one half of the switching frequency. This way, the attenuation would not affect the grid frequency while effectively dampening harmonics at the switching frequency. [23] The resonance frequency of the LCL filter can be calculated as

$$f_0 = \frac{1}{2\pi}\sqrt{\frac{L_1 + L_2}{L_1 L_2 C}} \tag{29}$$

4.4 Coupled inductors

The efficiency of an interleaved multiphase DC-DC converter increases when the filter inductance increases since the reduced current ripple allows for e.g. reduced magnetic losses. The output current ripple of a DDC is reduced via interleaved control methods but the inductor current ripple remains unchanged. However, increasing the filter inductance deteriorates the transient response of the DDC. A coupled inductor offers a solution to the problem. The coupled inductor works as a nonlinear inductor in a phase-shifted switching network, i.e. the equivalent inductance of the circuit is different in steady state and during transient behavior due to magnetic coupling of the windings. The design of the coupled inductor aims to achieve a high steady-state inductance L_{ss} and a low transient inductance L_{tr}. [6][22]

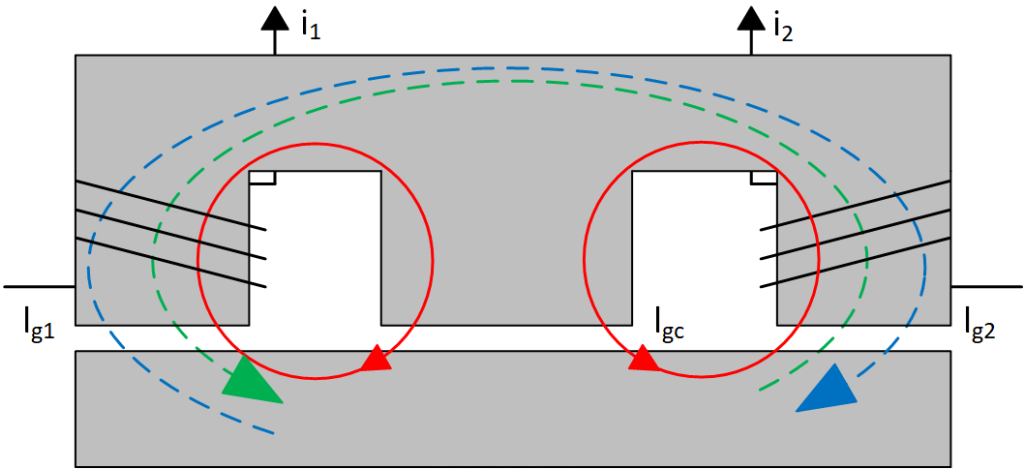

Figure 23: The two-phase coupled inductor structure and flux paths.

Coupled inductors consist of multiple windings wound around the same core, similar to transformers. As such, the model of the coupled inductor is similar to the transformer. Figure 23 shows the two-phase coupled inductor structure. In the figure, the solid red lines represent the leakage fluxes of both coils, and the dotted lines represent the coupling fluxes. In coupled inductors, the flux generated by the current of one coil also links to the adjacent coils.

The phenomenon is called mutual inductance M and can be expressed as

$$M = \alpha L \tag{30}$$

where L is the self-inductance of the coupled coil and α is the coupling coefficient. The coupling coefficient is a measure of magnetic coupling between the windings. The values of the coupling coefficient lie between -1 and 1. A negative value of α indicates inverse coupling and positive value of α indicates non-inverse coupling between the windings. For non-coupled inductors $\alpha = 0$. The voltages and currents of the two-phase coupled inductors are related by the following equations. [1] [22]

$$\begin{cases} u_1 = L_1 \dfrac{di_1}{dt} + M \dfrac{di_2}{dt} \\ \\ u_2 = L_2 \dfrac{di_2}{dt} + M \dfrac{di_1}{dt} \end{cases} \tag{31}$$

Figures 24 and 25 show the current and voltage waveforms for both coupled inductor and non-coupled inductor of a two-phase Buck converter for $D < 0.5$ and $D > 0.5$. The waveforms of coupled inductor are marked with solid line. The phase-shifted switching network causes the equivalent inductance of the coupled inductor to change during the switching cycle. The reason for this is the different current and voltage combinations seen in Figures 24 and 25. The equivalent inductances L_{eq1}, L_{eq2} and L_{eq3} are needed to analyze the steady state and the transient behavior of the circuit and they are determined by both mutual and self-inductances and the duty cycle. [22] [25]

The steady-state inductor current ripple affects the converter efficiency. Therefore, the steady-state inductance can be defined using inductor current ripple as a criterion. As seen from Figure 24, the equivalent inductance L_{eq1} determines the inductor current ripple in steady state when $D < 0.5$. Correspondingly from Figure 25 can be deduced that the equivalent inductance L_{eq3} determines the inductor current ripple in steady state when $D > 0.5$. Hence, the steady-state inductance for these two operation ranges is determined as:

$$\begin{cases} L_{ss} = L_{eq1} = \dfrac{L^2 - M^2}{L + \dfrac{D}{D'} M}, & D < 0.5 \\ \\ L_{ss} = L_{eq3} = \dfrac{L^2 - M^2}{L + \dfrac{D'}{D} M}, & D > 0.5 \end{cases} \tag{32}$$

where $D' = 1 - D$. [26]

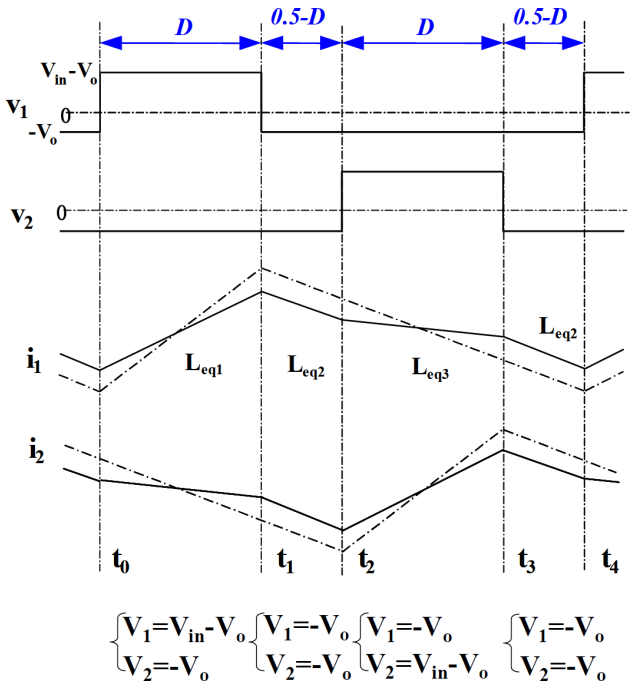

Figure 24: Current and voltage waveforms for coupled and non-coupled inductors of a Buck converter when $D < 0.5$. Dashed lines represent the current waveforms of two non-coupled inductors. [22]

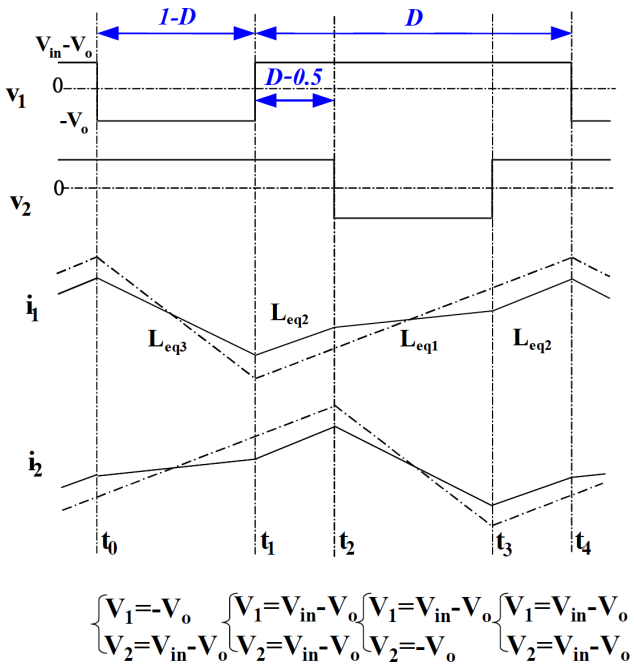

Figure 25: Current and voltage waveforms for coupled and non-coupled inductors of a Buck converter when $D > 0.5$. Dashed lines represent the waveforms of two non-coupled inductors. [22]

The transient criterion equals the slew rate of the current during transient response. Figure 26 shows the system transient response to a duty cycle perturbation ΔD. Red line corresponds the waveform changes due to ΔD. It can be derived that L_{eq2} determines the transient response of the phase current in two-phase Buck converter. Therefore, the transient inductance L_{tr} equals L_{eq2} and is determined as:

$$L_{tr} = L_{eq2} = L + M < L \tag{33}$$

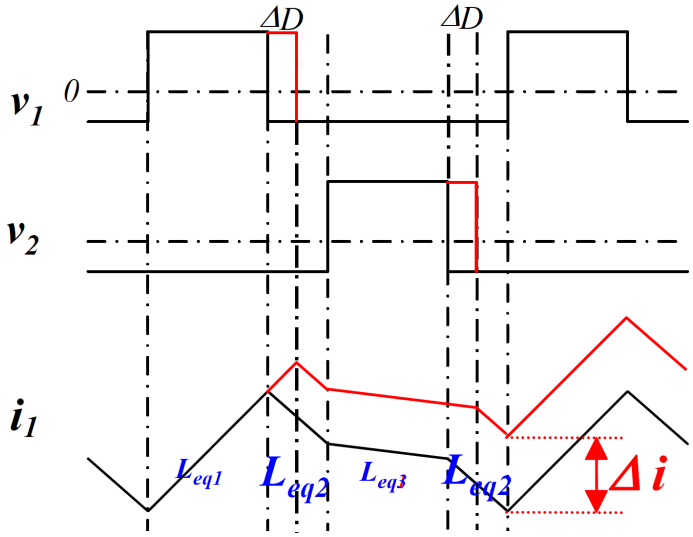

Figure 26: Transient voltage and current waveforms for the two-phase coupled-inductor of a Buck converter. [22]

Equation (33) shows that the inversely coupled inductor reduces the transient inductance, and therefore, increases the the transient performance of the multiphase Buck converter. The inversely coupled inductor may also increase the steady-state inductance of the multiphase Buck converter. [22]

The above analysis and equations are valid for the two-phase coupled inductor and may be extended for n-phase coupled inductors. Appendix A presents the analysis and derivation of equations for a three-phase coupled inductor. The analysis is divided into three cases based on the duty cycle D.

The coupled inductor is designed to have reduced steady-state current ripple while exhibiting a similar transient response as the non-coupled inductor. This is achieved by having a large $|\alpha|$ and $L_{tr} = L_{nc}$. Therefore, the ratio of the peak-to-peak current ripples of the n-phase coupled inductor and the non-coupled inductor can be expressed as the ratio of the transient inductance and the steady-state inductance. [22]

$$\frac{I_{c,p2p}}{I_{nc,p2p}} = \frac{L_{tr}}{L_{ss}} \tag{34}$$

The ratio of L_{tr} and L_{ss} can be determined as the figure of merit (FOM) of the multiphase Buck converter with a coupled-inductor. Figure 27 shows this FOM as a function on duty cycle D. The maximum ripple reduction depends on the steady-state duty cycle and the number of coupled phases. A greater phase current ripple reduction is achieved with a wider range of duty cycles as the number of coupled phases increases. [22]

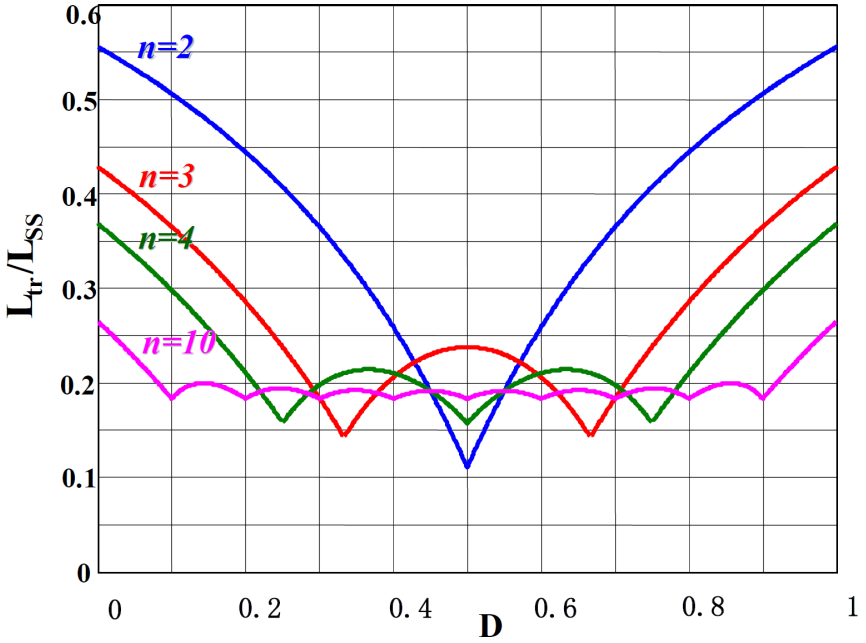

Figure 27: The ratio of the L_{tr} to L_s as a function of the duty cycle D for a various number of phases n with coupling coefficient $\alpha = -0.8$. [22]

5 Filter design

The objective of this thesis is to find a filter design that fulfills the requirements stated in Table 1 while achieving better power density and lighter design. These requirements originate from a reference design with an inductance of 360 μH.

This chapter presents three filter designs based on the topologies described in Chapter 4, forming equations for calculating the component values of each filter topology and verifying the performance of the solutions through simulation. Finally, example inductor designs of the presented topologies are compared.

Table 1: Filter inductor design requirements.

Requirements		
B_{max}	0.8	Maximum allowed flux density [T]
f_{sw}	4000	Switching frequency [Hz]
L_{min}	150	Minimum filter inductance (per phase) [μH]
I_o	600	Rated output current of DC-DC converter [A]
$i_{o,p2p}$	60	Maximum allowed output current ripple (10 %)[A]
U_{DC}	1000	Rated input voltage of DC-DC converter [V]
x_{yoke}	210	Core length of the filter inductor [mm]
y_{yoke}	110	Core width of the filter inductor [mm]
z_{tot}	260	Total height of the filter inductor [mm]

5.1 LC and LCL filter

LC and LCL are higher-order filter topologies that have good ripple attenuation even with small inductance values. However, selecting sufficient component values for LC and LCL filters is more complicated compared to the simple L filter. In order to fulfill the attenuation requirements and not bring harmful oscillations to the system, the filters need to be designed carefully. [23] Also, the inductance value must be large enough to keep the converter in CCM with the rated output current.

In this section, the sufficient component values for LC and LCL filters are derived. The simulation model to verify filter performances is presented and simulations results are discussed.

5.1.1 AC equivalent circuit analysis for LC and LCL filter

In order to simulate the performance of LC and LCL filter topologies with DDC, the component values for both topologies need to be calculated. Equation (8) that describes the output current ripple of an n-phase interleaved DC-DC converter with L filter, is not applicable with higher-order topologies.

Figure 28 shows the equivalent circuit of the DDC and LCL filter. A DC voltage source E_{Batt} and a series resistance R_{Batt} form the battery system acting as a load of the DDC. The voltage over the battery system is lower than the input voltage of the DC-DC converter. The equivalent circuit is similar to the LC filter apart from the second inductance L_{f2}.

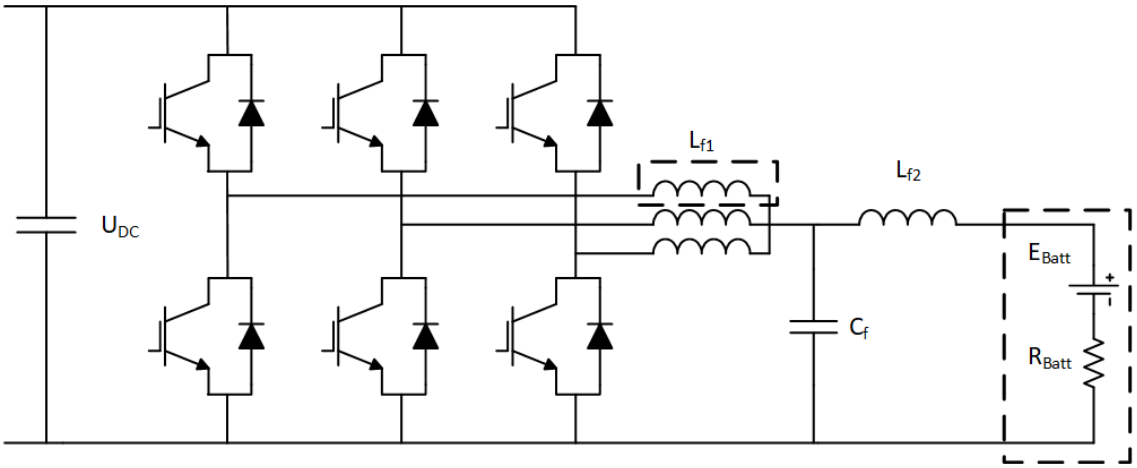

Figure 28: Three-phase interleaved DC-DC converter with LCL output filter and battery system.

Using AC analysis, it is possible to determine the output current ripple for both converter topologies, LC, and LCL. Figure 29 describes the conversion of the three-phase equivalent circuit to a single-phase counterpart. By means of Fourier analysis, it is possible to divide the rectangular input voltage into its spectral components. The frequency component of the voltage waveform at triple the switching frequency is sinusoidal. Therefore, the input voltage seen by the filter structure can be modelled as a sinusoidal voltage source E_n. The battery DC voltage source is shorted and the output current ripple is calculated using the following equations:

$$\hat{E}_{n,j} = \left| \frac{2}{\pi} U_{DC} \sin((1 - nD)\pi) \frac{1}{2j+1} \right| \tag{35}$$

$$Z_{tot} = s_n L_{f1} + \frac{R_{Batt} + s_n L_{f2}}{s_n C_f \left(s_n L_{f2} + R_{Batt} + \dfrac{1}{s_n C_f} \right)} \tag{36}$$

$$i_{o,p2p} = 2 \left| \frac{\hat{E}_{n,j}}{Z_{tot}(s_n)} \times \frac{\dfrac{1}{s_n C_f}}{s_n L_{f2} + R_{Batt} + \dfrac{1}{s_n C_f}} \right| \tag{37}$$

where j is the harmonic number ($j = 0$ for n times the switching frequency component), $s_n = 2\pi n f_{sw}$ is the Laplace variable, and Z_{tot} is the total impedance of the

equivalent circuit. For LC filter $L_{f2} = 0$. For a more accurate result, more harmonic components can be included for the calculation (j = 1,2,...). The output current ripple can be determined with sufficient accuracy by the nf_{sw} component, i.e., $j = 0$.

Figure 30 shows the the calculated battery current ripple for LC filter over L_{f1} and C_f. The battery current ripple can be adjusted by changing the inductance and capacitance values. [2]

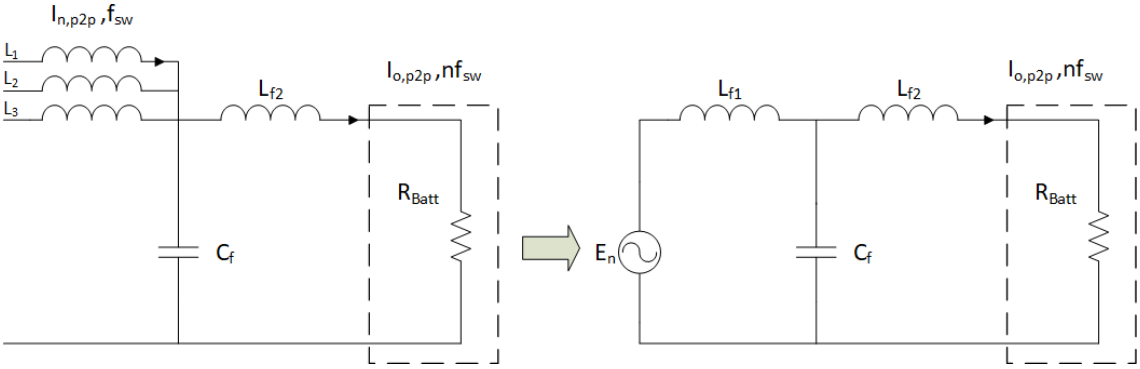

Figure 29: A single-phase equivalent circuit of the DC-DC converter and LCL filter. In the model and calculations $L_{f1} = L_1 = L_2 = L_3$. [2]

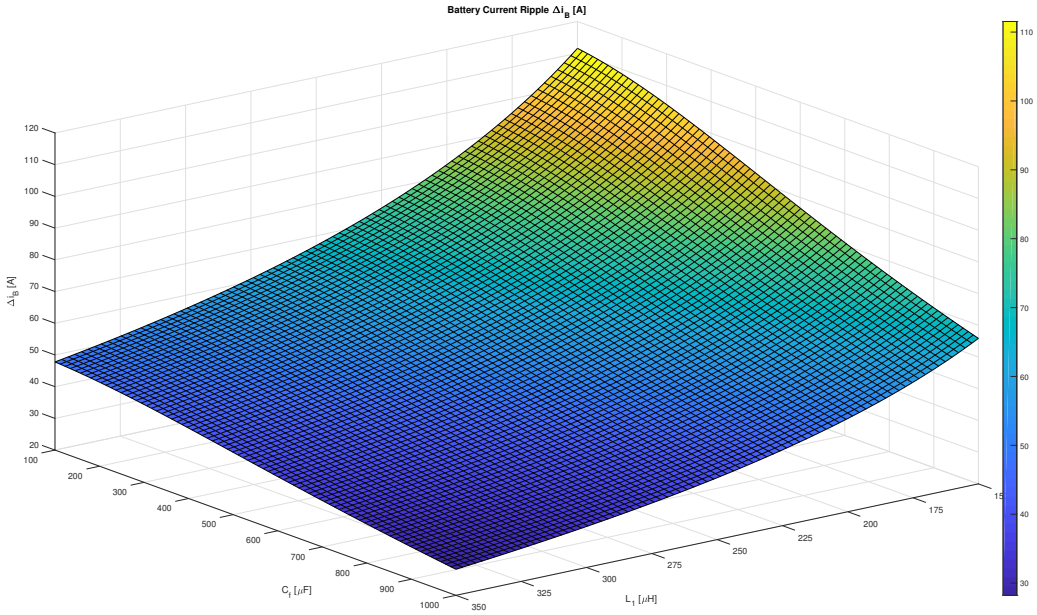

Figure 30: Battery current ripple over L_{f1} and C_f for DDC and LC filter. In the graph $L_{f1} \in]150, 350[$, $C_f \in]100, 1000[$, and $\Delta i_B \in]20, 120]$.

Higher-order filters may cause harmful resonances to the converter circuit. Thus, resonance frequency of the filter is an important design variable. A rule of thumb is that the resonance frequency should be under half of the total switching frequency, here $f_0 < 6$ kHz. However, in this thesis even 7.5 kHz resonance frequency is considered acceptable. When calculating the resonance frequency of the filter circuit, L_{f1} acts as three parallel connected individual inductors.

5.1.2 Simulation of LC and LCL filters

The performance of the dimensioned LC and LCL filters was verified through simulation. The software used for circuit simulations is ANSYS Simplorer. The simulation model presented in Appendix B corresponds to the equivalent circuit in Figure 28. All components in the model are assumed to be ideal; only the battery system has a series resistance R_{Batt} of 18.5 mΩ. All simulations were conducted with $D = 0.5$ since it maximizes the output current ripple of the DDC.

In the model, the input of the DDC is an ideal DC voltage source. In a real-life application this could be e.g., a DC intermediate circuit of a frequency converter. Modeling an intermediate circuit as an ideal DC source is sufficient since only the steady-state behavior of the circuit is considered. It can also be assumed that the inductor currents are below the saturation point. Therefore the inductance value remains constant throughout the simulations.

Table 2: Simulated current ripple of the LC filter compared to the calculated value. ($U_{DC} = 1000$ V, $D = 0.5$ and $f_{sw} = 4$ kHz)

$L_{f1}[\mu\text{H}]$	$C_f[\mu\text{F}]$	$I_{n,p2p}$ [A]	$I_{o,p2p}$ [A]	$I_{o,p2p}$ (calculated) [A]
290	300	215.7	60.3	53.8
260	465	240.6	59.1	54.6
205	805	305.2	58.3	55.0
180	1000	347.6	57.4	54.9

The simulation results for the LC filter are presented in Table 2. The simulated peak-to-peak values are predictably higher than the calculated ones. The reason for this is that only the harmonics at n multiples of the switching frequency were included in the calculations, as discussed in Chapter 5.1.1. This estimation creates a difference of approximately 10 % between the calculated and simulated values. Figure 31 shows the amplitudes of the output current spectral components. It is noticeable that the amplitude of the 12 kHz component is very close to half of the calculated ripple value. There is also ripple components at multiples of 12 kHz. According to Figure 31, the highest harmonic component of the output current is 36 kHz with an amplitude of approximately 1 A.

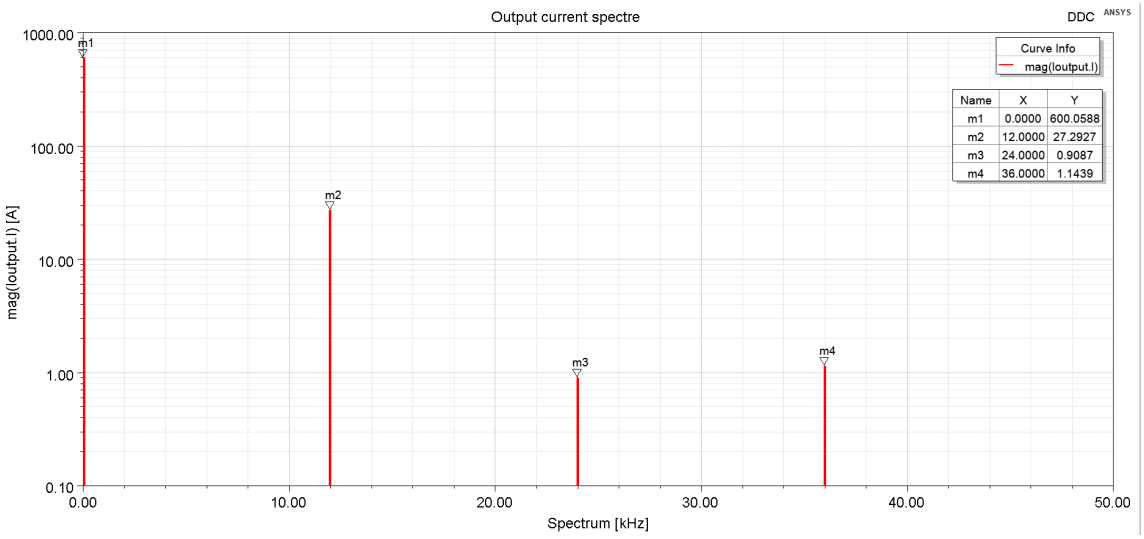

Figure 31: LC-filter output current spectre with $L_{f1} = 180$ μH and $C_f = 1000$ μF. Amplitudes from left to right: 600 A at DC, 27.3 A at 12 kHz, 0.9 A at 24 kHz and 1.1 A at 36 kHz.

Figure 32 shows the output and inductor currents of the DDC and the LC filter circuit. It can be seen that the output current waveform and peak-to-peak values are very similar in all simulated filters. However, the inductor current peak-to-peak values differ significantly from each other. The lower the inductance value of the LC filter, the higher the inductor current ripple. From this, we can conclude that the filter inductance value drastically affects the capacitance required in order to limit the current ripple within the allowed range.

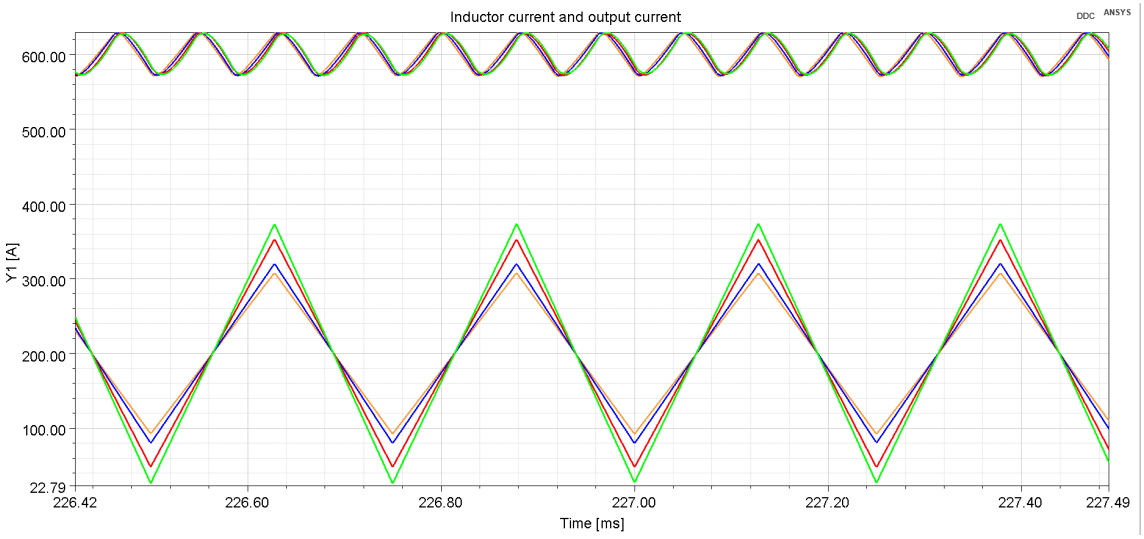

Figure 32: Simulated output current and inductor currents of the LC filter circuit. Corresponding component values of the waveforms: green: $L_{f1} = 180$ μH and $C_f = 1000$ μF, red: $L_{f1} = 205$ μH and $C_f = 805$ μF, blue: $L_{f1} = 260$ μH and $C_f = 465$ μF, orange: $L_{f1} = 290$ μH and $C_f = 300$ μF.

Table 3 shows the simulation results of the LCL filter. Similar to the case of the LC filter, the simulated peak-to-peak values are higher than the calculated ones, for the previously discussed reason. As seen from the table, all simulated current ripples are below 10 % of the nominal output current. Output current spectrum of LCL filter is shown in Figure 33. Comparing the output current ripple calculated with $L_{f1} = 180$ μH, $L_{f2} = 5$ μH, $C_f = 105$ μF and two times the amplitude of the 12 kHz component in the spectrum, we find that the values are close to each other.

Table 3: Simulated current ripple of the LCL filter compared to the calculated value. ($U_{DC} = 1000$ V, $D = 0.5$ and $f_{sw} = 4$ kHz)

$L_{f1}[\mu\text{H}]$	$L_{f2}[\mu\text{H}]$	$C_f[\mu\text{F}]$	$I_{n,p2p}$ [A]	$I_{o,p2p}$ [A]	$I_{o,p2p}$ (calculated) [A]
200	7	70	314.5	53.9	48.2
180	5	105	348.8	54.0	47.8
170	10	55	371.0	56.1	48.0

The simulated output current and inductor currents for the LCL filter with $L_{f1} = 180$ μH, $L_{f2} = 5$ μH, $C_f = 105$ μF are presented in Figure 34. As seen from the figure, there is a small amount of oscillation at the resonance frequency in the output current of the LCL filter. It can be noticed that the resonance frequency component is also visible in Figure 33, which suggests that the resonance frequency component is amplified in the circuit. As the components in the simulation model are ideal and there are no damping resistances, even small disturbances may lead to strong resonance in the circuit. By adding component and wire resistances of a few mΩ to the model, the resonance is suppressed.

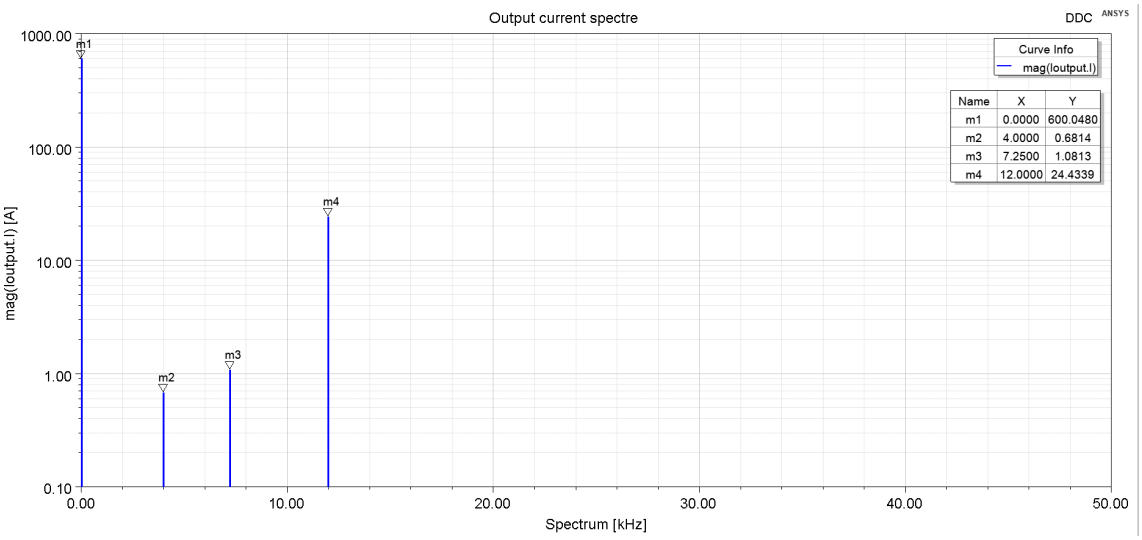

Figure 33: LCL-filter output current spectre with $L_{f1} = 180$ μH, $L_{f2} = 5$ μH and $C_f = 105$ μF. Amplitudes from left to right: 600 A at DC, 0.7 A at 4 kHz, 1.1 A at 7.25 kHz and 24.4 A at 12 kHz.

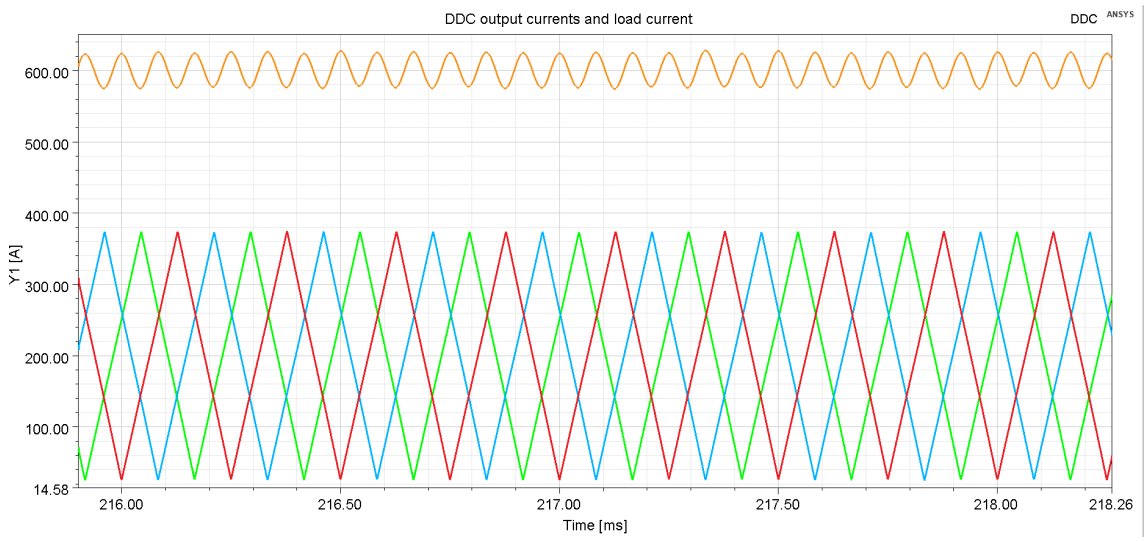

Figure 34: Simulated output current and inductor currents of the LCL filter circuit with $L_{f1} = 180\ \mu H$, $L_{f2} = 5\ \mu$H and $C_f = 105\ \mu$F.

As for the LCL filter output current spectrum, it can be observed that the switching frequency component (4 kHz) is interestingly nonzero. According to the Chapter 2.3, the 4 kHz component should disappear from the spectrum in the summation of the phase currents. Usually, nonidentical phase inductance values lead to unequal amplitudes of the phase currents. When the current values of the phases are not equal, the summation is imperfect and current ripple components at the switching frequency appear in the output current instead of the expected number of phase times the switching frequency. The phenomenon also increases the peak-to-peak value of the output current. In the LCL circuit, the source of the current imbalance is not the unequal inductance values but the voltage fluctuation of the filter capacitor. The capacitance of the LCL filter is considerably smaller compared to the LC filter, and thus the voltage ripple of the capacitor is higher in the LCL filter circuit. Also, in the simulation model of the LC filter circuit, the DC voltage source is parallel-connected to the filter capacitor. Therefore, the voltage ripple over the capacitor is reduced significantly.

As expected, the higher-order filters dampen higher harmonic frequencies effectively. Comparing the two spectrums in Figures 31 and 33, we notice more harmonic components in the LC filter spectrum. In the LCL output current spectrum, the highest frequency is three times the switching frequency, i.e., 12 kHz, while for LC it is 36 kHz. It can be deducted from the results that even a small inductance of 5 to 10 μH significantly reduces the required filter capacitance value for the same output ripple. Therefore, for the same L_{f1}, the filter capacitance can even be ten times smaller, compared to the capacitance of the LC filter circuit.

In conclusion, both LC and LCL filter topologies lead to a considerable reduction of the phase inductance value due to more effective attenuation of high-frequency

components. They also change the output current waveform compared to the L filter. The explanation for this is that the sum of the phase currents is a triangular wave and generates sinusoidal voltage ripple in the capacitor, which in turn results in sinusoidal current ripple on the load side.

5.2 Coupled inductor

Coupled inductor has multiple advantages over the higher-order topologies. With careful design of a coupled inductor, it is possible to extend the ripple reduction from the output current to the phase currents and improve the transient performance of the system. [22]

The following chapters discuss dimensioning and simulation of a three-phase coupled inductor. First, the parameter values for the equivalent circuit are calculated. The simulation model and results are discussed in the next chapter.

5.2.1 Dimensioning coupled inductor

Dimensioning a coupled inductor filter for DDC requires a different approach than conventional LC and LCL filters. The objective of the design was to keep the transient response of the circuit unchanged while reducing the phase current ripple. The output current ripple should not exceed 10 % of the nominal output current. The reduction of the phase current ripple reduces both the switching losses of the semiconductors and the required cooling capacity of the power module.

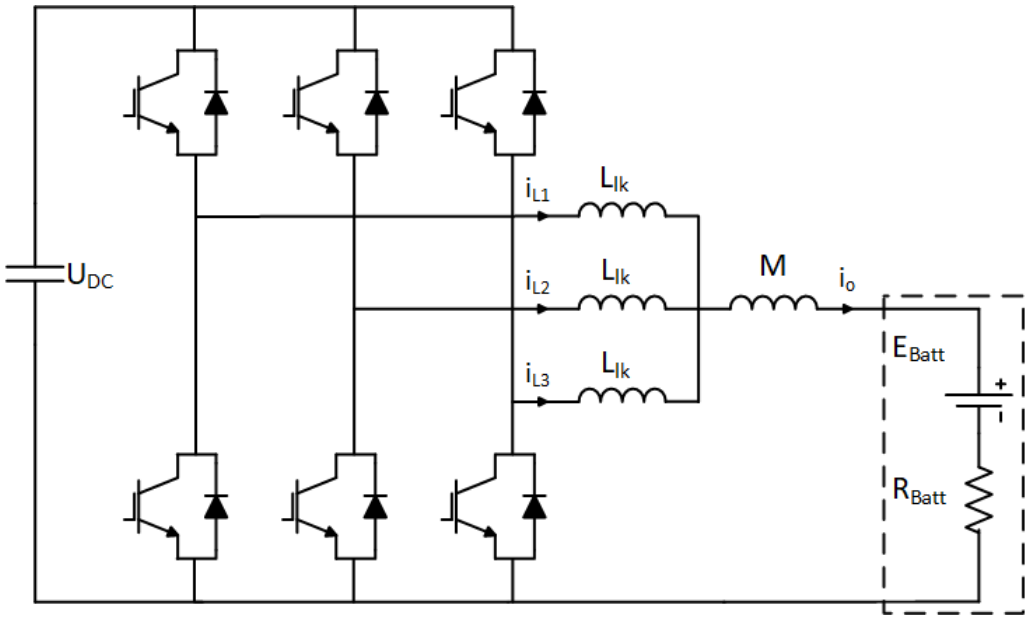

Figure 35: Three-phase interleaved DC-DC converter with a coupled inductor output filter and a battery system. To keep the output current ripple and the transient response of the system unchangeable, $L_{lk} = L_{tr}$.

Figure 35 shows the equivalent circuit of the DDC with a three-phase coupled inductor output filter and a load. The coupled inductor is modeled as an ideal three-phase transformer with three leakage inductances L_{lk} and mutual inductance M. The structure of the coupled inductor is symmetrical, i.e., mutual M and leakage inductances L_{lk} of each phase are equal. For inverse coupling, $M < 0$. Similar to the LC and LCL filter circuits, the load consists of a DC voltage source E_{Batt} and a series resistance R_{Batt}.

In order to analyze the steady-state and transient behavior of the circuit, we need to calculate the corresponding steady-state and transient inductances L_{ss} and L_{tr} as in Chapter 4.4. For a three-phase coupled inductor, the analysis is divided into three parts based on the value of D: $0 \leq D < 1/3$, $1/3 \leq D < 2/3$, and $2/3 \leq D < 1$. The equations for calculating steady-state and transient inductances are introduced here. The derivation of the equations is presented in Appendix A.

For $0 \leq D < 1/3$

$$L_{ss} = \frac{(L-M)(L+2M)}{L + \left(1 + \dfrac{2D}{D'}\right) M}, \tag{38}$$

for $1/3 \leq D < 2/3$

$$L_{ss} = \frac{(L-M)(L+2M)}{L + \left(\dfrac{2}{3DD'} - 1\right) M}, \tag{39}$$

and for $2/3 \leq D < 1$

$$L_{ss} = \frac{(L-M)(L+2M)}{L + \left(1 + \dfrac{2D'}{D}\right) M} \tag{40}$$

To keep the transient response of the circuit equal to the response of the non-coupled reference design, the transient inductance should equal the non-coupled inductance, i.e., $L_{tr} = L_{nc} = 360\ \mu$H. The transient inductance of the three-phase coupled inductor is

$$L_{tr} = L + 2M \tag{41}$$

Unlike the steady-state inductance L_{ss}, the transient inductance L_{tr} does not change with the duty cycle D. This can be explained as follows. Figure 36 shows the transformation of the three-phase coupled inductor circuit to its single-phase counterpart. The equivalent inductance of the single-phase circuit equals three parallel-connected transient inductors. Therefore, it can be deduced that the transient inductance of each phase equals the leakage inductance of each phase, i.e. $L_{lk} = L_{tr}$. As a result, the output current ripples of the three-phase coupled inductor filter and the non-coupled reference design are equal since $L_{lk} = L_{tr} = L_{nc}$. [6][22]

The mutual inductances and self-inductances needed for the calculations can be derived from the coupling coefficient definition for the three-phase coupled inductor.

$$M = \frac{\alpha L}{2} \tag{42}$$

Substituting this to Equation (41), we get

$$L = \frac{L_{tr}}{\alpha + 1} = \frac{L_{nc}}{\alpha + 1} \tag{43}$$

We may conclude that while the leakage inductance L_{lk} remains constant, the mutual inductance M changes with respect to the coupling coefficient α. Also, the steady-state inductance L_{ss} seen by the circuit and thus the phase current ripple change with respect to D and α.

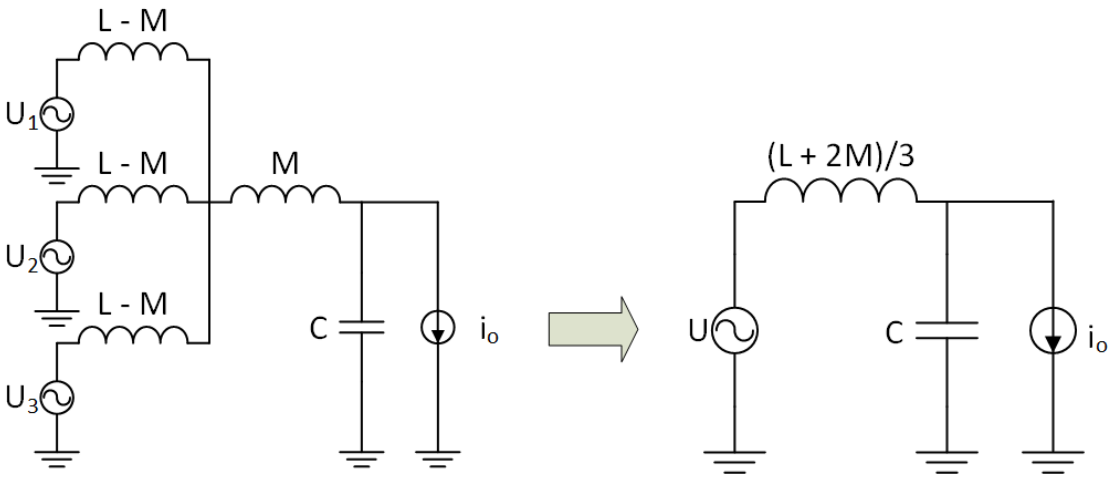

Figure 36: Transformation from a three-phase coupled inductor circuit to a single-phase equivalent circuit. In the model $U = U_1 = U_2 = U_3$.

5.2.2 Simulation of the coupled inductor

The performance of the output filter consisting of a coupled inductor was verified through simulation. The software used for circuit simulations is ANSYS Simplorer. The simulation model corresponds to the equivalent circuit presented in the previous chapter. The filter inductances are modeled using mutual M and leakage inductances L_{lk}. The leakage inductance L_{lk} of the model equals the transient inductance L_{tr} calculated in the previous chapter, and the mutual inductance M is defined by the self-inductance and coupling coefficient. As opposed to the LC and LCL filters simulation model, the equivalent inductance of the filter is not constant throughout the simulations since the values of the coupling coefficient α and duty cycle D are varied in the simulations. Only inversely coupled inductors are simulated, i.e., $\alpha \leq 0$. As equations in Chapter 5.2.1 suggests, the steady-state inductance L_{ss} seen by the

circuit depends on both the duty cycle D and the coupling coefficient α. Therefore, the phase current ripples should change when one or both of these values change.

Other components of the model are the same as in LCL and LC filters outlined in Chapter 5.1.2. The simulated current ripples of the coupled inductor are compared to the simulated values of the non-coupled inductor of 360 μH. More details of the simulation model are presented in Appendix C.

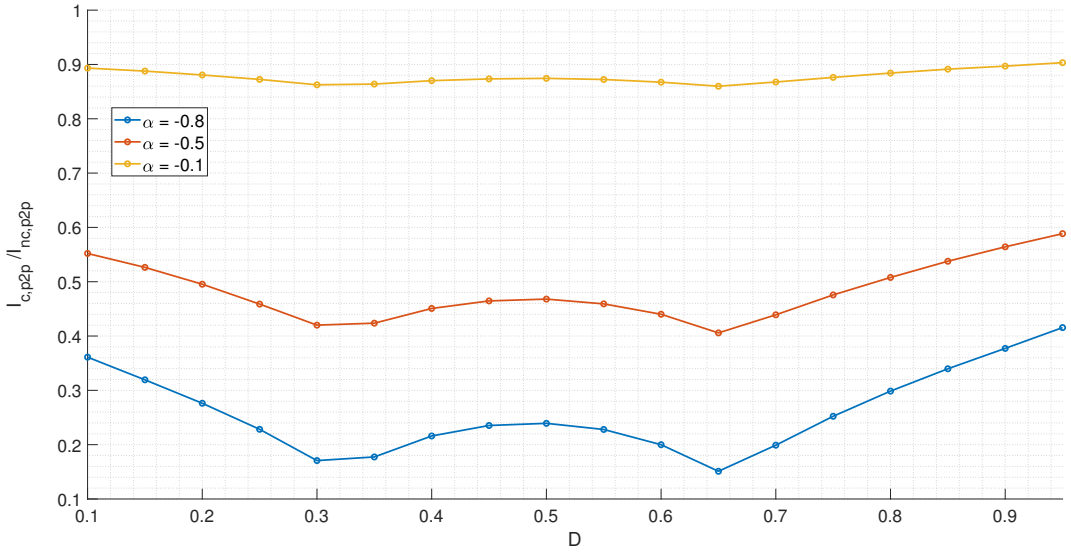

Figure 37: Current ripple ratio of the coupled inductor to the non-coupled inductor vs. the duty cycle D with different coupling coefficient values α.

Figure 37 shows the effect of the duty cycle D (x-axis) to the relative phase current ripple reduction (y-axis), for different values of the coupling coefficient α. The closer α is to -1, i.e., the more ideal the coupling is, the better the ripple reduction is compared to the non-coupled inductor. It can be seen from the figure that for a three-phase interleaved DC-DC converter, the ripple reduction is most effective with duty cycle D values of 1/3 and 2/3. The notches in the curve are steeper the closer α is to -1.

Figure 38 shows the simulated coupled inductor currents. The waveforms of $\alpha = -0.05$ and $\alpha = -0.25$ resemble the waveforms of the non-coupled inductor. Instead, the waveforms of $\alpha = -0.6$ and $\alpha = -0.95$ are clearly different from the non-coupled case. As expected, the output current waveform and ripple remains unchanged in all simulation cases when α varies from 0 to -1. Instead, the phase current ripples and waveforms change significantly as α approaches -1. As the coupling coefficient α approaches -1, the frequency of the phase current triples and peal-to-peak value is reduced by approximately 85% compared to the non-coupled reference design.

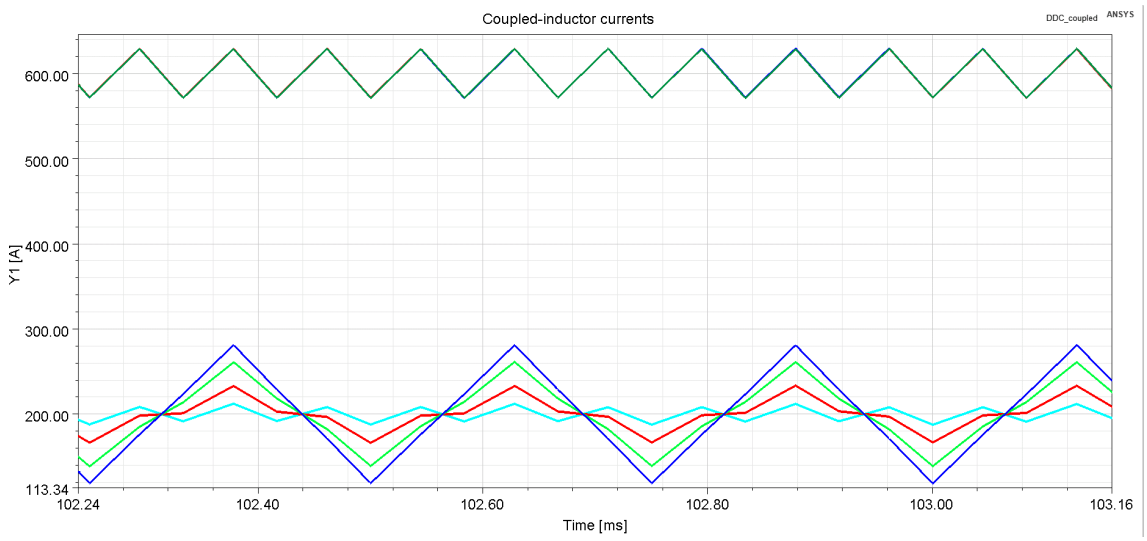

Figure 38: Coupled inductor current waveforms: turquoise $\alpha = -0.95$, red $\alpha = -0.6$ light green $\alpha = -0.25$ and dark blue $\alpha = -0.05$ and $D = 0.5$.

Figure 39 shows the simulated inductor phase currents with $\alpha = -0.95$ and $D = 0.5$. As the coupling coefficient α approaches -1, the phase currents are nearly equal and in-phase. Since the output current is a sum of these nearly equal phase currents, the output current ripple does not change compared to the non-coupled case. However, a high coupling coefficient decreases the phase current ripples and increases the ripple frequency.

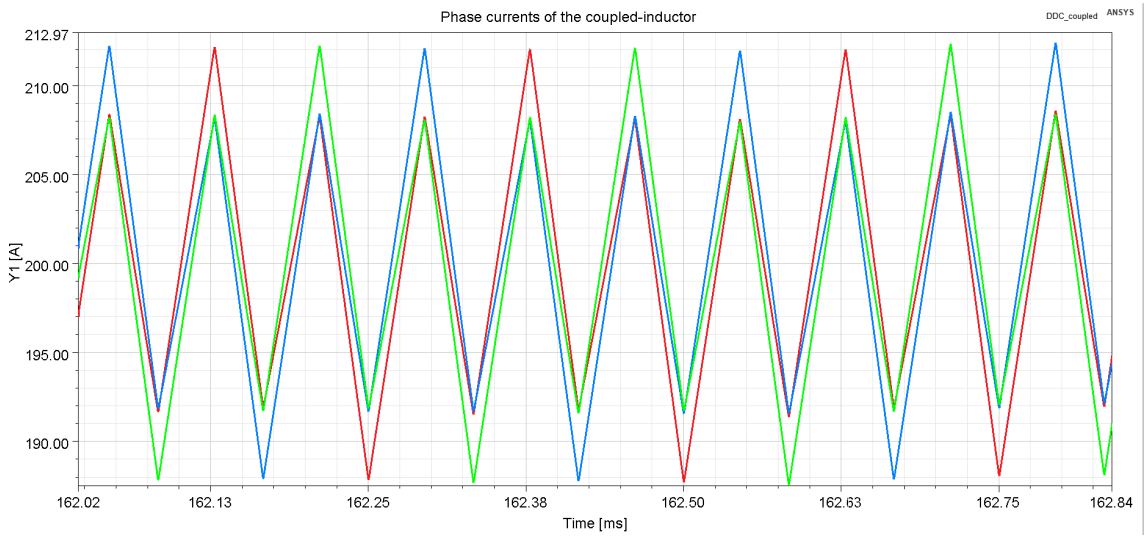

Figure 39: Coupled inductor phase currents with $\alpha = 0.95$. and $D = 0.5$.

In addition to the coupling coefficient α, the duty cycle D plays an important role in the relative phase current ripple reduction. Figure 40 shows the effect of the coupling coefficient α to the phase current ripple reduction, for different values of the duty cycle D.

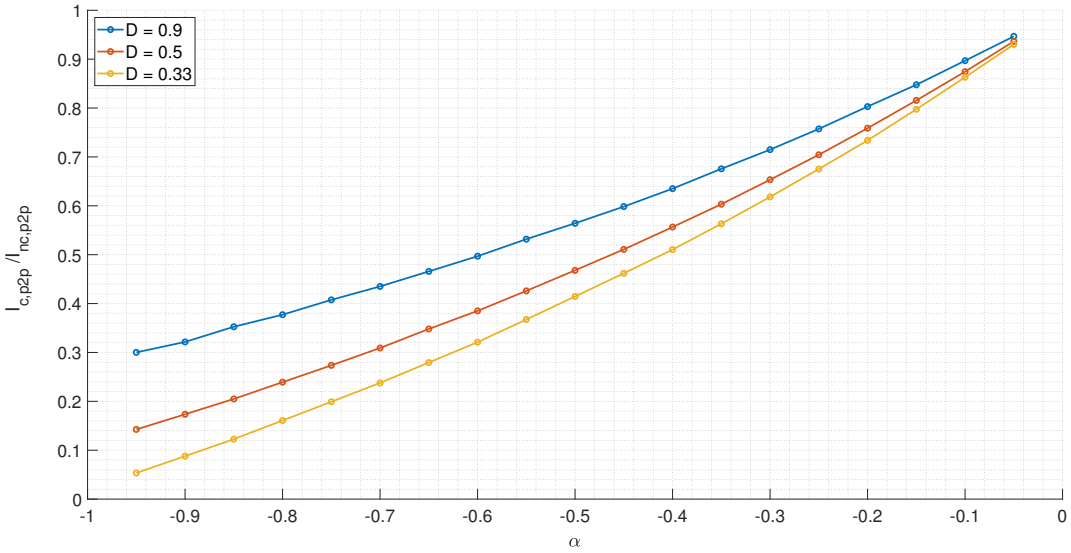

Figure 40: Current ripple ratio of the coupled inductor to the non-coupled inductor vs. the coupling coefficient α with different duty cycles D.

The figure supports the theory that the most effective ripple reduction is achieved in local minimums 1/3 and 2/3 as the FOM is at its minima.

It can be concluded that the simulated current ripple ratios follow closely to the theoretical ones. The curves of Figure 37 resemble the FOM of $n = 3$ in Figure 27. It can be seen from the graphs that, compared to the two-phase coupled inductor discussed in Chapter 4.4, it is possible to achieve larger current ripple reduction in a wider duty cycle range with the three-phase coupled inductor. Also, Figure 37 shows that when the coupling coefficient α approaches zero, the duty cycle D has a lesser effect to the ripple reduction. It can be deduced from the simulation results that the equivalent circuit and the simulation model describe the operation of a three-phase coupled inductor accurately.

5.3 Comparison of different output filter designs

This chapter focuses on the design of a first filter inductor, i.e. phase inductor of the DDC. A classic design approach of an inductor is discussed. A reference design is used as the basis for the new design. After this, the cost-effectiveness and quality of the new design is evaluated. Also a design proposal for coupled inductor is briefly discussed and reviewed.

General magnetic laws and theory presented in Chapter 3 are involved in the design process. In addition to this, many different approaches may be taken in order to optimize the design depending on the application. The objective of this work was to design such an output filter that fulfills the requirements stated in Table 1 while achieving better power density. Therefore, the physical size and weight of the component played an important role in the design.

A flow chart of typical inductor design procedure is illustrated in Figure 41. The process starts from the electrical values. Inductance value L, peak current I_p and RMS current are determined, e.g., based on calculations and simulations. After this, a suitable core geometry and material are chosen. At this point, the core dimensions are determined. When designing the windings of the inductor, a few rules need to be considered. The number of turns should respect the following inequality to avoid saturation of the core.

$$B_{sat} N A_c > L I_p \tag{44}$$

The inequality ensures that core saturation will not occur in the expected current range of the component. In turn, the number of turns N affects on the winding style and wire diameter selection. The windings should fit in the window area of the core. After this, the required air gap length to achieve the desired inductance value is determined. As a rule of thumb, if the total air gap length l_g exceeds 5% of the smallest core dimension, the gap needs to be divided into several subgaps in final design to avoid fringing effect. [27]

The calculated winding and core losses serve as evaluation criteria for the made design choices. If the calculated winding losses are too big, either the diameter of the used wire or the number of windings need to be changed. Current density ($\mathrm{A}/(\mathrm{mm}^2)$) in the wire is also a good indicator for possible thermal challenges. In case of big core losses, the core material could be changed or the size of the core increased. Since the accurate calculation of losses is difficult and often leads to approximations, a thermal characteristics of the component should be simulated to validate the results. After this, in-circuit testing is conducted for a prototype inductor to verify the design. In conclusion, the design process requires iteration to find the most optimal core and winding solution. [27]

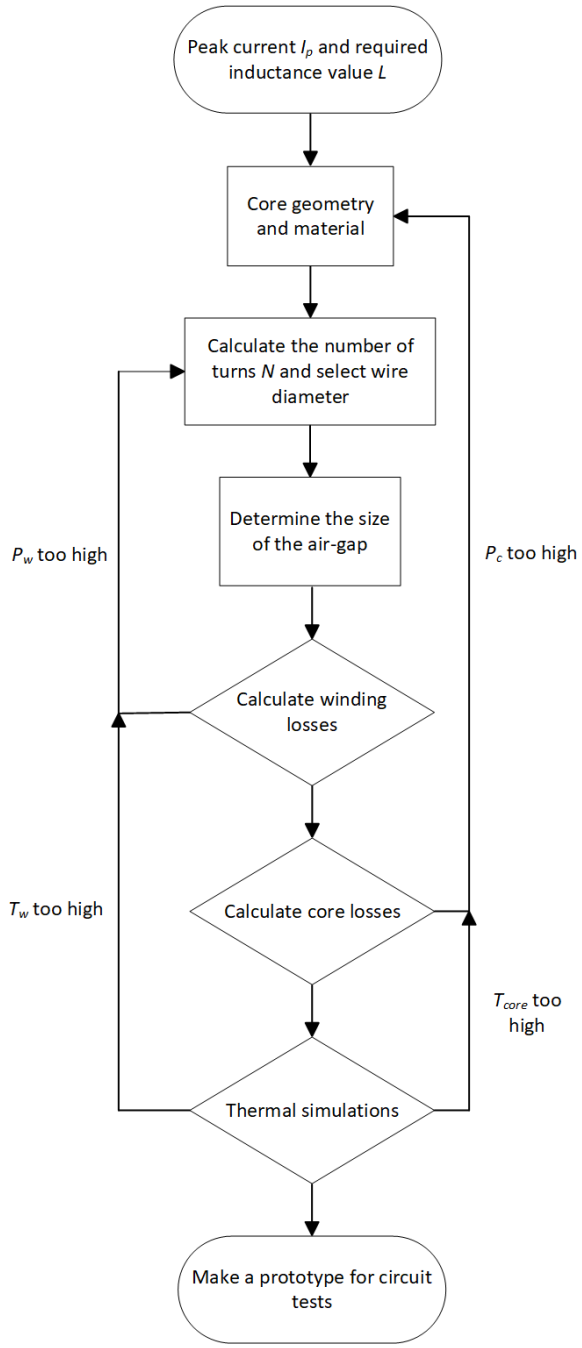

Figure 41: A flow chart of the inductor design procedure.

According to the simulation results of Chapter 5.1.2, a phase inductance value of 180 μH is sufficient for LC and LCL filters. Also, it happens to be exactly half the reference inductance value. An interesting comparison can be made by studying how halving the inductance value effects on the design when used power range remains unchanged. Therefore, an inductance value of 180 μH was chosen for the example design. The simulated current peak value for $L = 180$ μH was approximately 375 A, but 400 A was used in design in order to allow a margin of error.

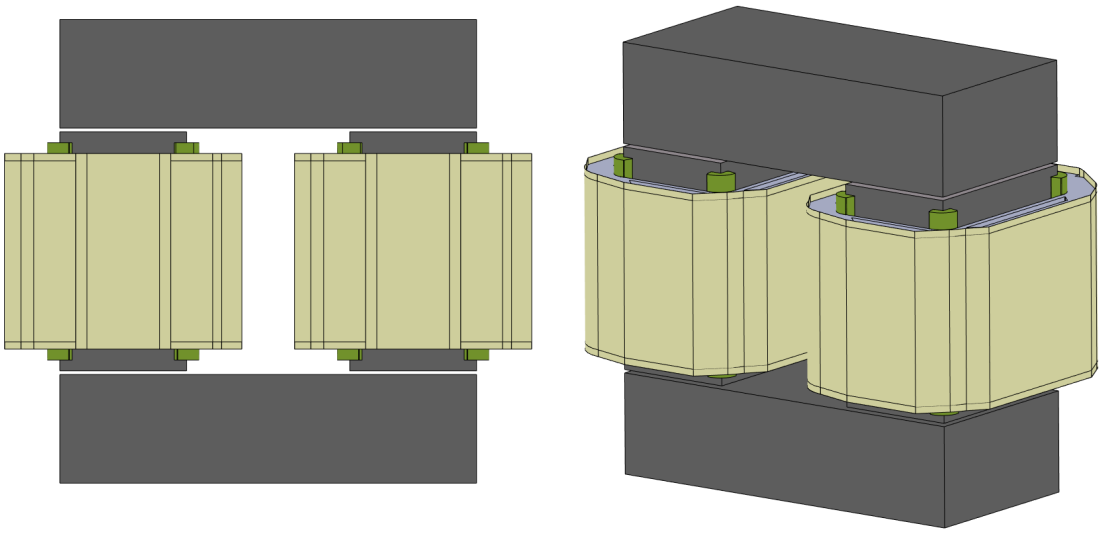

Figure 42: Example inductor design for $L = 180$ μH.

The reference design of 360 μH worked as a basis of the new design. Thus, the core geometry and material were chosen to be equal to those of the reference inductor. Also the wire shape and thickness were chosen to match the windings of the reference design. This also simplified the comparison of the advantages and challenges of the new inductor design. Figure 42 illustrates the example design of 180 μH.

Table 4: Design variables of the new inductor design of $L = 180\mu$H and difference to the reference design of $L = 360\mu$H.

DV	Description	Value	Value Δ %
x_{yoke}	Core length of the filter inductor	180 mm	-14.3 %
y_{yoke}	Core width of the filter inductor	90 mm	-18.2 %
z_{tot}	Total height of the filter inductor	230 mm	-11.5 %
l_g	Total air gap length	16.5 mm	-8.3 %
A_c	Cross-sectional area of the core	4500 mm^2	-37.1 %
N	Number of turns per coil	23	-14.8 %
m_L	Total mass on the inductor	29	-38.3 %

Table 4 compares the example design to the reference design of 360 μH. As seen from the table, halving the inductance value reduces the physical size of the component significantly. Smaller dimensions lead to reduction of both winding and core material cost. However, the losses of the new design are considerably increased. The reason for this is that the approximately 93 % increase in inductor current ripple leads to increased peak value of the magnetic flux, and thus, increased core loss. Resulting core loss is almost double compared to the reference design. Considering semiconductor switches, increased current ripple reduces the turn-on losses while increasing the turn-off losses. In any case, the current stress of the semiconductors increases.

All previously mentioned factors lead to increased requirements for cooling capacity. A study of an LCL filter design for a three-phase PFC rectifier came to a similar conclusion: there is always a trade-off between the volume and losses in filter design. [28]

Figure 43 introduces an example structure of a three-phase coupled inductor. The structure resembles a traditional three-phase inductor apart from two extra pillars on both sides. In a coupled inductor structure, a part of the flux generated by one winding goes through other windings. Since the windings are inversely coupled, the fluxes generated in the other windings are partially canceled out. The mutual inductance of the core is determined by the ratio of the flux going through the other windings to the total flux. [26] Additional limbs on both sides of the structure provide a path for the leakage flux that does not go through the inner three limbs. In order to achieve strong coupling between the windings, the magnetic reluctances of the outer pillars should be greater than those of the inner limbs. This can be achieved by adding larger air gaps to the outer pillars or by reducing the cross-sectional area. It is also possible to use a different magnetic material for the outer pillars.

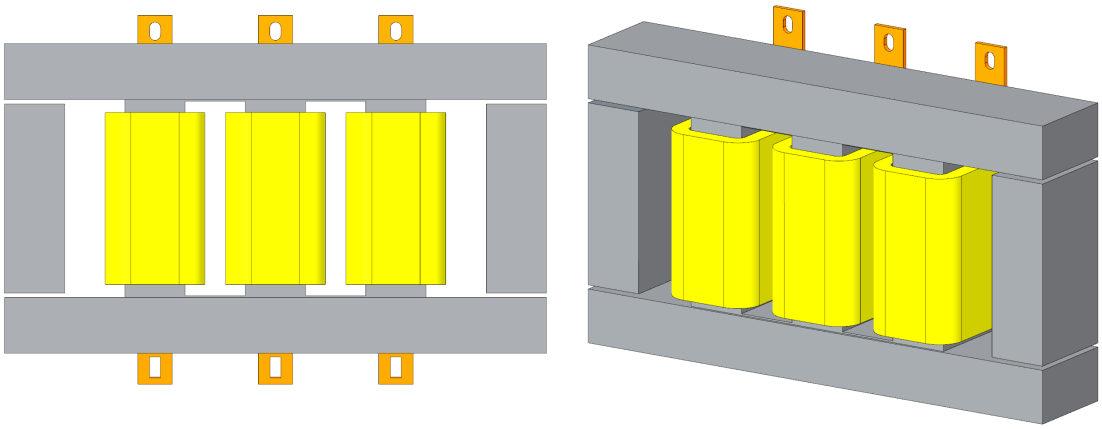

Figure 43: An example structure for coupled inductor.

The coupled inductor structure shown in Figure 43 is not entirely symmetrical. However, if each limb has an air gap, it can be assumed with sufficient accuracy that the air gap reluctances dominate in the reluctance network. Then, the asymmetry caused by the different lengths of the magnetic paths can be neglected. The reluctance network of the coupled inductor core is simplified to the form shown in Figure 44. Since the reluctance network is symmetrical, it holds $\Re_{g,1} = \Re_{g,2} = \Re_{g,3}$ and $N_1 i_{L1} = N_2 i_{L2} = N_3 i_{L3}$. The approximation could form a basis for the design of a coupled inductor.

The proposed structure is not the only possible option. Another possible symmetrical structure for an n-phase coupled inductor is proposed in [29]. The structure consists of n radially distributed legs around one center leg. The coupling factor between the windings can be adjusted by changing the air gap length of the center leg.

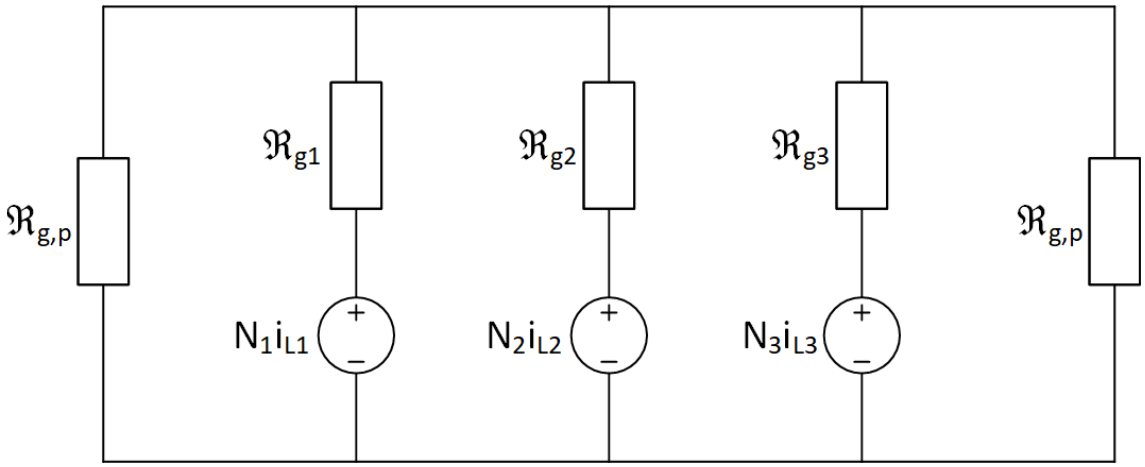

Figure 44: The reluctance network of a coupled inductor structure. For symmetrical coupled-inductor structure it holds $\Re_{g,1} = \Re_{g,2} = \Re_{g,3}$ and $N_1 i_{L1} = N_2 i_{L2} = N_3 i_{L3}$.

At any rate, designing the coupled inductor requires careful planning in order to maximize its performance. Manufacturing of the component may be difficult and therefore expensive.

All in all, a comparison between different filter topologies (LC and LCL) and a coupled inductor is difficult. LC and LCL filters allow for smaller inductance at the expense of high inductor current ripple and the resulting excessive power loss, whereas the usage of a coupled inductor leads to smaller phase current ripples while maintaining the same output ripple level. Adding a DC film capacitor to the filter circuit and halving the filter inductance value is the most cost-effective solution, compared to the reference filter. The capacitor is small and inexpensive component compared to an inductor. As for the LCL filter, the circuit suffers from unwanted resonances, and would also require an additional inductor design. Even though the inductor could have an air core and be rather small, an extra component and design would increase the total cost of the filter. Therefore, the LC filter is a more cost-effective solution compared to both L and LCL filters. With regard to the coupled inductor design, the technology requires further investigation and simulation of the magnetic behavior for different core structures.

6 Conclusions

This thesis studied the output filter of a bi-directional interleaved three-phase DC-DC converter (DDC). In order to minimize the output current ripple and the consequent losses, the filter inductance is required to be sufficiently large. However, the size and cost of the filter increase with the inductance. In addition to this, a large filter inductance deteriorates the transient response of the DDC.

In a three-phase interleaved DC-DC converter, the filter inductor consists of three parallel-connected inductors. The interleaved control method and parallel-connected separate inductors reduce the size and weight of a single component. Also, the control method reduces the output current ripple, and thus, the required filter inductance. Therefore, a further reduction of filter inductance while maintaining the same output current ripple level requires a different design approach.

The purpose of this study was to find the best output filter design for DDC with respect to cost-efficiency and power density. The literature review presents the theoretical background about the DC-DC converters, electromagnetic laws, inductor structure, magnetic materials and filter topologies. The review discusses the losses in both switch-mode power converters and magnetic components.

Based on the literature review, three filter designs were chosen for simulations: LC, LCL and the coupled-inductor. Electrical values for simulations were determined using a single-phase equivalent circuit. The simulation results for LC filter and the coupled-inductor were promising while the LCL filter suffered from unwanted resonance and current imbalance. Based on the simulations results, an example design for a 180 μH inductor was made using the reference design of 360 μH as a basis for the new design. An example structure for the coupled-inductor was analysed. Finally, the designs were compared against each other and the most cost-effective solution was presented.

Comparing LC and LCL filter topologies and the coupled-inductor filter proved to be difficult. While the LC filter is the most cost-effective solution, it comes with its own set of problems. The reduction of the filter inductance by 50 % results in a 93 % increase in inductor current ripple, and thus, a significant increase in core loss. In filter design, the whole system should be considered to achieve an ideal result. This study confirms that there is always a trade-off between the volume and losses in filter design.

The coupled-inductor showed promising results in the simulations. However, the proposed structure requires further investigation and simulation of the magnetic flux paths. The reluctance network presented in the previous chapter could be a starting point for the design, however core materials for different parts need to be selected based on the magnetic simulations and more accurate reluctance model. The losses in the coupled-inductor and the transient behavior need to be studied and simulated as well. Also, other alternative structures with inverse magnetic coupling should be considered.

This thesis did not include thermal modeling or simulations of the proposed 180 μH filter design. Loss calculations of the filter give an initial approximation of the thermal behavior which should be verified either by a simulation or a prototype for in-circuit tests. At any rate, significantly increased core losses require a more efficient cooling system compared to the reference design. The reference design of 360 μH formed a basis for the new design to simplify the comparison. By choosing a different core geometry, core material and windings, it is possible to optimize the design with respect to the losses. Still, optimizing some parameters in the system deteriorate other parts of the system.

References

[1] Mohan, N. *Power Electronics: A First Course.* Hoboken, N.J.: John Wiley & Sons, 2011. ISBN: 978-1-118-07480-0.

[2] Jung, M. *Optimized design of DC-DC converter LC output filter for EV battery charging applications in terms of defined battery current and voltage ripple as well as overall system efficiency.* 2016 18th European Conference on Power Electronics and Applications (EPE'16 ECCE Europe), Karlsruhe, pp. 1-8, 2016.

[3] Jung, M., Lempidis, G., Hölsch, D. & Steffen, J. *Optimization considerations for interleaved DC-DC converters for EV battery charging applications, in terms of partial load efficiency and power density.* 2015 17th European Conference on Power Electronics and Applications (EPE'15 ECCE-Europe), pp. 1-9, 2015.

[4] Mohan, N., Robbins, W.P. & Undeland, T.M. *Power Electronics: Converters, Applications, and Design.* 3rd ed. Hoboken, NJ: John Wiley & Sons, 2002. ISBN: 0-471-22693-9.

[5] Kyyrä, J. *Hakkuriteholähteet.* Course handout. Espoo, Aalto-yliopiston Sähkötekniikan korkeakoulu, 2013.

[6] Lee, J.P., Cha, H., Shin, D., Lee, K.J., Yoo, D.W., & Yoo, J.Y. *Analysis and Design of Coupled Inductors for Two-Phase Interleaved DC-DC Converters.* Journal of Power Electronics, vol. 13, no. 3, pp. 339–348, 2013.

[7] Lai, J.& Nelson, D. J. *Energy Management Power Converters in Hybrid Electric and Fuel Cell Vehicles.* Proceedings of the IEEE, vol. 95, pp. 766-777, 2007.

[8] Kim, S. -M.& Sul, S. -K. *Control of Rubber Tyred Gantry Crane With Energy Storage Based on Supercapacitor Bank.* IEEE Transactions on Power Electronics, vol. 21, pp. 1420-1427, 2006.

[9] Baliga, B.J. *Advanced high voltage power device concepts.* New York, NY: Springer, 2011.

[10] Niiranen, J. *Tehoelektroniikan komponentit.* 4th ed. Helsinki, Otatieto, 2007.

[11] Salmia, T. *Taajuusmuuttajaan liitettävän superkondensaattorienergiavaraston tehonsiirron mitoitus.* Master's thesis, Aalto University, Department of Electrical Engineering, Espoo, 2010.

[12] Volke, A. & Hornkamp, M. *IGBT modules: Technologies, driver and application.* 3rd ed. Munich, Infineon Technologies AG, 2017.

[13] Bierhoff, M. H. & Fuchs, F. W. *Semiconductor losses in voltage source and current source IGBT converters based on analytical derivation.* 2004 IEEE 35th Annual Power Electronics Specialists Conference (IEEE Cat. No.04CH37551), Aachen, Germany, Vol.4., pp. 2836-2842, 2004.

[14] Van den Bossche, A. & Valchev, V.C. *Inductors and Transformers for Power Electronics.* 1st ed. Boca Raton, CRC Press, 2005. ISBN: 1574446797.

[15] Mahafugur Rahman, F.M. *Converter-side inductor design for a grid-connected converter equipped with an LCL filter.* Master's thesis, Aalto University, Department of Electrical Engineering, Espoo, 2016.

[16] Kazimierczuk, M.K. *High-Frequency Magnetic Components.* Somerset: John Wiley & Sons, Incorporated, 2014.

[17] McLyman, C. W. T. *Transformer and inductor design handbook.* 4th ed. Boca Raton, Florida: CRC Press, 2011.

[18] Lounia, M. *Magneettisten komponenttien suunnittelu.* 2nd ed. Helsinki, ABB Oy Drives, Technology, 2008.

[19] Mühlethaler,J. *Modeling and Multi-objective Optimization of Inductive Power Components* PhD dissertation, Swiss Federal Institute of Technology Zurich, Department of Information Technology and Electrical Engineering, Zurich, 2012.

[20] Thorborg, K. *Power electronics.* New York: Prentice Hall, 1988. ISBN: 0-13-686593-3.

[21] *EconoPACK^{TM}+ module with Trench/Fieldstop IGBT4 and Emitter Controlled 3 diode and PressFIT / pre-applied Thermal Interface Material* FS500R17OE4DP, Infineon, 2016. Accessed on: Apr. 15, 2020. [Online]. Available: Infineon.com

[22] Dong, Y. *Investigation of Multiphase Coupled-Inductor Buck Converters in Point-of-Load Applications.* PhD dissertation, Virginia Polytechnic Institute and State University, Blacksburg, Virginia, 2009.

[23] Bauer, J., Lettl, J. & Linhart, L. *Comparison of Different Filter Types for Grid Connected Inverter.* Progress in Electromagnetics Research Symposium Proceedings, Marrakesh, Morocco, 2011, p. 1426-1429.

[24] Atmaca, Ö., Erol, E., Kamal, T. & Karabacak, M. *Design of an H-Bridge Bidirectional DC–DC Converter with LCL Filter for High Power Battery Applications.* 2019 1st Global Power, Energy and Communication Conference (GPECOM), Nevsehir, Turkey, 2019, pp. 238-241.

[25] Wong, P., Wu, Q., Xu, P., Yang, B. & Lee, F.C. *Investigating coupling inductors in the interleaving QSW VRM.* APEC 2000. Fifteenth Annual IEEE Applied Power Electronics Conference and Exposition (Cat. No.00CH37058), New Orleans, LA, USA, 2000, pp. 973-978 vol.2.

[26] Wong, P. *Performance Improvements of Multi-Channel Interleaving Voltage Regulator Modules with Integrated Coupling Inductors.* PhD dissertation, Virginia Polytechnic Institute and State University, Blacksburg, Virginia, 2001.

[27] Tanaskovic, M. *Development of a Magnetic Component Design Environment.* Master's thesis, Swiss Federal Institute of Technology Zurich, Department of Information Technology and Electrical Engineering, Zurich, 2011.

[28] Muhlethaler, J., Schweizer, M., Blattmann, R., Kolar, J. W. and Ecklebe, A. *Optimal Design of LCL Harmonic Filters for Three-Phase PFC Rectifiers.*, IEEE Transactions on Power Electronics, vol. 28, no. 7, pp. 3114-3125, July 2013.

[29] Kang, T. & Suh, Y. *Optimized Coupling Factor Design of Multiple-Phase Coupled Inductor for Minimum Inductor Current Ripple Operation in EV Charger Systems.* 2017 IEEE 3rd International Future Energy Electronics Conference and ECCE Asia (IFEEC 2017 - ECCE Asia), Kaohsiung, 2017, pp. 1178-1183.

Appendix A

This appendix describes the derivation of the equations used for calculating simulation parameters for coupled inductor. The contents of this appendix are based on the work done in [22].

The current and voltage equations for a three-phase coupled inductor are:

$$\begin{cases} u_1 = L_1\dfrac{di_1}{dt} + M\dfrac{di_2}{dt} + M\dfrac{di_3}{dt} \\ u_2 = L_2\dfrac{di_2}{dt} + M\dfrac{di_1}{dt} + M\dfrac{di_3}{dt} \\ u_3 = L_3\dfrac{di_3}{dt} + M\dfrac{di_1}{dt} + M\dfrac{di_2}{dt} \end{cases} \tag{A.1}$$

where $L1$, L_2 and L_3 are the self-inductances for each phase and M is the mutual inductance between two phase inductors. For a symmetrical coupled inductor it holds that $L_1 = L_2 = L_3$.

Figure A.1 shows the voltage waveforms and the current i_1 waveform of a three-phase coupled inductor in steady-state when $1/3 \leq D < 2/3$. In total, six switching intervals occur during one switching cycle. We can consider the six inductances $L_{eq1} - L_{eq6}$, each corresponding to a switching interval, equivalent to those in non-coupled inductor case. For different voltage and current combinations shown in Figure A.1 six equivalent inductances can be derived:

$$L_{eq1} = L_{eq_3} = \frac{(L-M)(L+2M)}{L + \dfrac{D}{D'}M} \tag{A.2}$$

$$L_{eq2} = \frac{(L-M)(L+2M)}{L + \left(1 + \dfrac{2D}{D'}\right)M} \tag{A.3}$$

$$L_{eq4} = L_{eq6} = \frac{(L-M)(L+2M)}{L + \dfrac{D'}{D}M} \tag{A.4}$$

$$L_{eq5} = \frac{(L-M)(L+2M)}{L + \left(1 + \dfrac{2D'}{D}\right)M} \tag{A.5}$$

where $D' = 1 - D$.

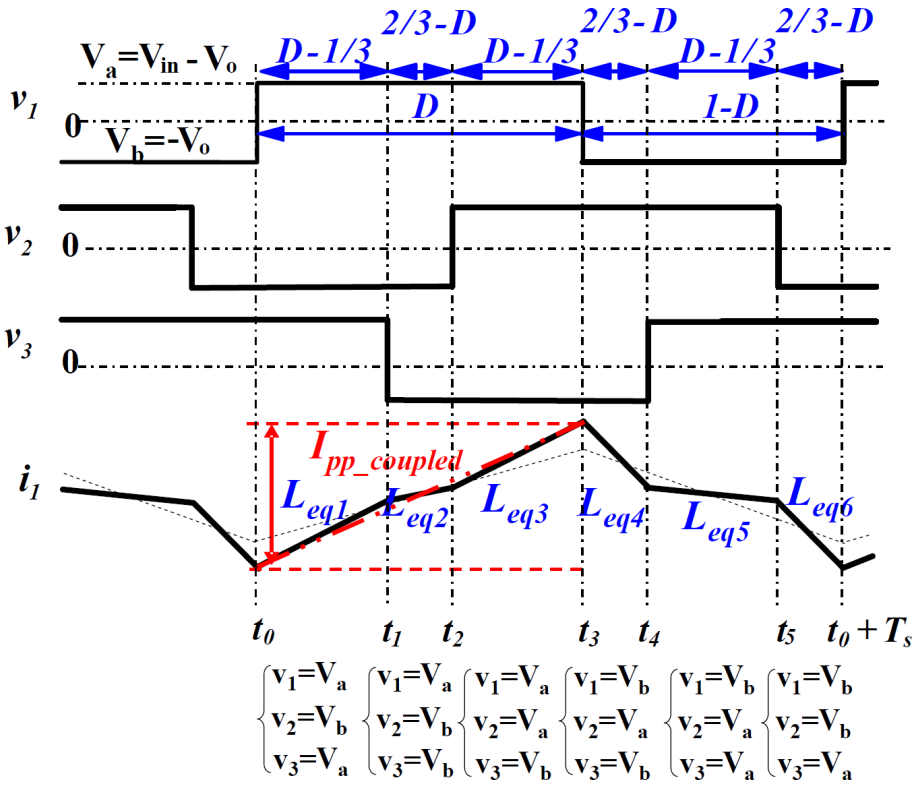

Figure A.1: Three-phase coupled inductor Buck converter current and voltage waveforms in steady-state when $1/3 \leq D < 2/3$. Solid line depicts actual current and voltage waveforms of the coupled-inductor, the black dashed line depicts the current waveform of a single non-coupled inductor and the red dashed line depicts the average current slope of a coupled inductor.

The steady-state inductance L_{ss} is determined by the phase current ripple. As seen from Figure A.1, unlike with the two-phase coupled inductor the peak-to-peak value of the phase current is not determined by one of the equivalent inductances. By defining the steady-state inductance as the inductance equivalent to that in the three-phase non-coupled inductor of a Buck converter, we get the average current slope depicted with red dashed line in Figure A.1. Using the average current slope, the steady-state inductance L_{ss} can be expressed as:

$$L_{ss} = \frac{1}{\frac{1}{L_{eq1}} \cdot \frac{2(D-1/3)}{D} + \frac{1}{L_{eq2}} \cdot \frac{2/3-D}{D}} = \frac{(L-M)(L+2M)}{L + \left(\frac{2}{3DD'} - 1\right) M} \tag{A.6}$$

The transient inductor current and voltage waveforms for three-phase coupled inductor Buck converter are shown in Figure A.2. The transient inductance is defined as the equivalent inductance which determines transient response to a duty cycle perturbation ΔD.

$$\frac{\Delta i}{T_{sw}} = \frac{\Delta D U_i n}{L_{tr}} \tag{A.7}$$

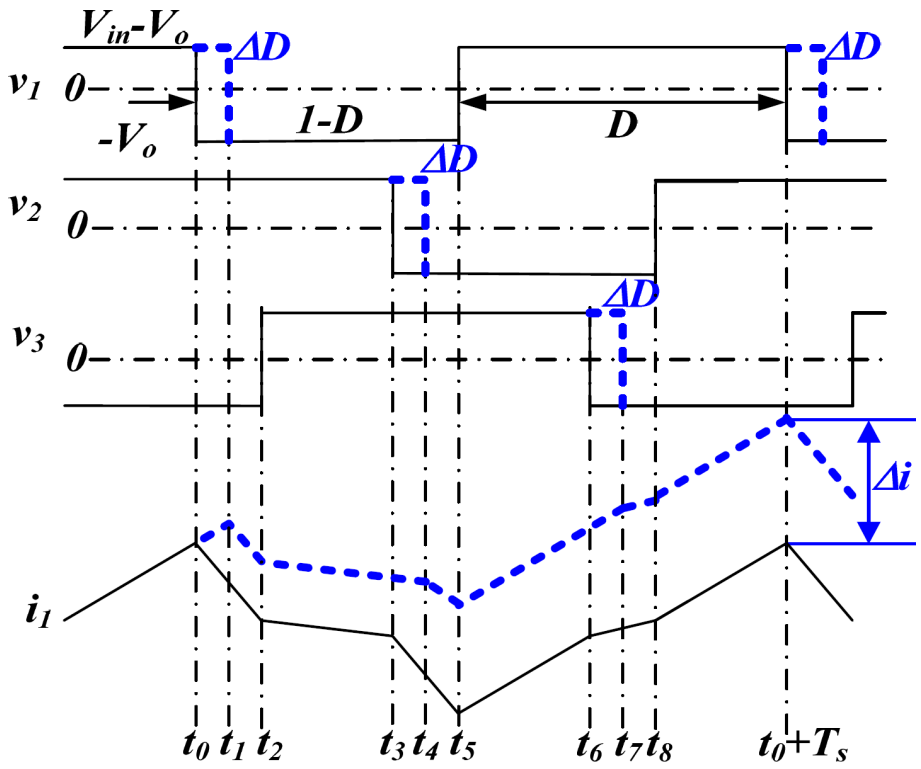

Figure A.2: Transient current and voltage waveforms for the three-phase coupled inductor with a Buck converter when $1/3 \leq D < 2/3$. The waveform changes caused by the duty cycle perturbation ΔD are marked with blue dashed line.

The current change Δi in switching cycle T_{sw} is

$$\Delta i = (L_{eq1} - L_{eq4})\Delta D \cdot T_{sw} + (L_{eq5} - L_{eq4})\Delta D \cdot T_{sw} + (L_{eq1} - L_{eq2})\Delta D \cdot T_{sw} \quad \text{(A.8)}$$

From Equations A.7 and A.8 can be derived

$$L_{tr} = L + 2M \quad \text{(A.9)}$$

Figure A.3 shows the steady-state voltage current waveforms of a three-phase coupled inductor when $2/3 \leq D < 1$. As in previous case, there are six equivalent inductances $L_{eq1} - L_{eq6}$ corresponding each switching interval. By substituting different voltage and current combinations shown in Figure A.3 into Equation (A.1), we get

$$L_{eq1} = L_{eq3} = L_{eq5} = L + 2M \quad \text{(A.10)}$$

$$L_{eq2} = L_{eq4} = \frac{(L - M)(L + 2M)}{L + \frac{D}{D'}M} \quad \text{(A.11)}$$

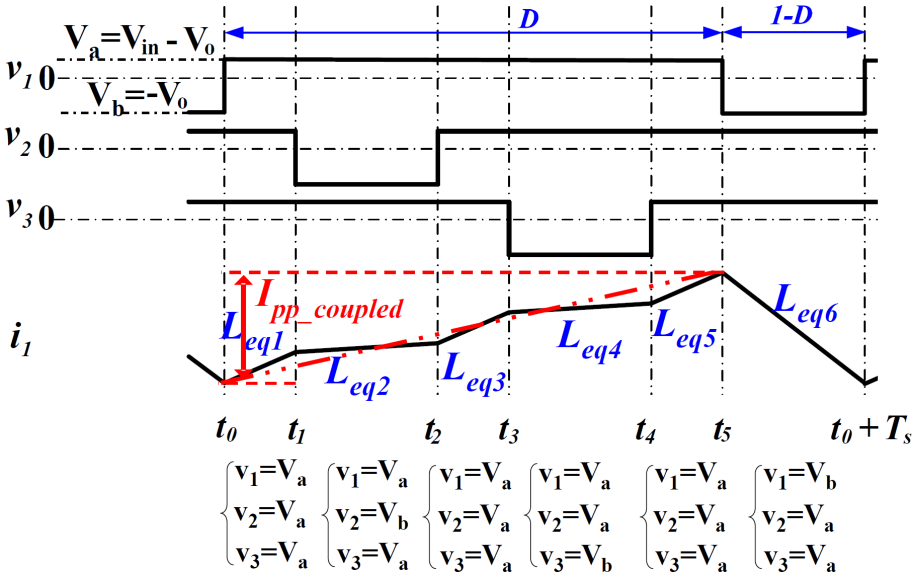

Figure A.3: Three-phase coupled inductor Buck converter current and voltage waveforms in steady-state when $2/3 \leq D < 1$. Solid line depicts actual current and voltage waveforms of the coupled-inductor and the red dashed line depicts the average current slope of a coupled inductor.

$$L_{eq6} = \frac{(L-M)(L+2M)}{L + \left(1 + \dfrac{2D'}{D}\right) M} \tag{A.12}$$

As seen from Figure A.3, the peak-to-peak value of the phase current can be determined by inductance L_{eq6}. Therefore the steady-state inductance is

$$L_{ss} = L_{eq6} = \frac{(L-M)(L+2M)}{L + \left(1 + \dfrac{2D'}{D}\right) M} \tag{A.13}$$

The transient inductor current and voltage waveforms for three-phase coupled inductor Buck converter are shown in Figure A.2. For Δi we get

$$\Delta i = (L_{eq1} - L_{eq6})\Delta D \cdot T_{sw} + (L_{eq1} - L_{eq2})\Delta D \cdot T_{sw} + (L_{eq1} - L_{eq2})\Delta D \cdot T_{sw} \tag{A.14}$$

By substituting this to Equation (A.8) we get

$$L_{tr} = L + 2M \tag{A.15}$$

The value of the transient inductance is the same as for $1/3 \leq D < 2/3$. This is also the leakage inductance of the three-phase coupled inductor. Therefore, it can be deducted the leakage inductance of the coupled inductor determines the transient performance of the three-phase coupled inductor Buck converter.

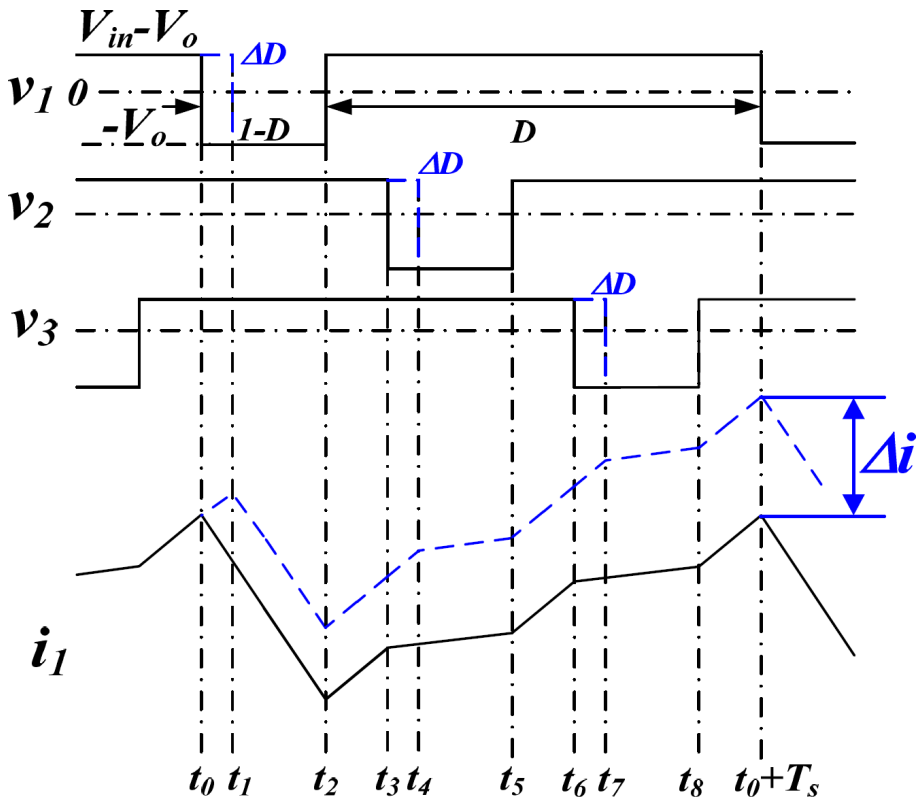

Figure A.4: Transient current and voltage waveforms for the three-phase coupled inductor with a Buck converter when $2/3 \leq D < 1$. The waveform changes caused by the duty cycle perturbation ΔD are marked with blue dashed line.

The derivation of equations for case $0 \leq D < 1/3$ are not presented here since it is the duplicate of the $2/3 \leq D < 1$ case. If D and D' are exchanged in Equation (A.6), we get the steady-state inductance equation for the $0 \leq D < 1/3$ case.

Appendix B

This appendix describes the simulation model used in simulation for DDC with LC and LCL filters in Chapter 5.1.2. The software used for circuit simulations is ANSYS Simplorer. The LCL filter in the model consists three identical parallel-connected inductors, common filter capacitance and second filter inductor. Figure B.2 shows the parallel connected filter inductors. An ideal DC voltage source and a resistor act as the load for the DDC. Simulated filter parameters are listed in Chapter 5.1.2 and Table B.1 presents the remaining values used in the simulations.

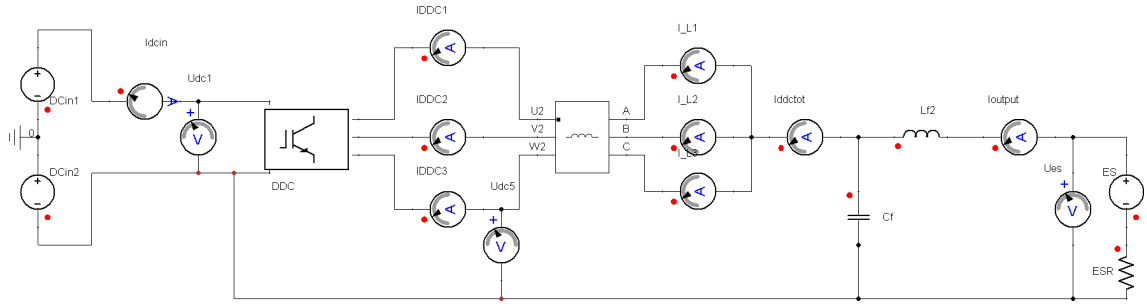

Figure B.1: Simulation model for coupled inductor LC and LCL filter circuits.

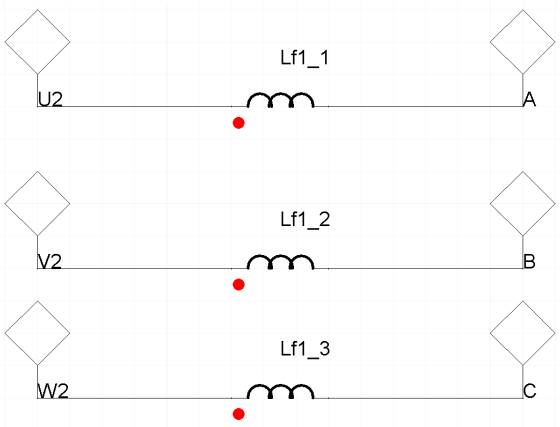

Figure B.2: Parallel-connected filter inductors.

Table B.1: LC and LCL filter simulation model variables.

Variable	Value	Description
DCin1	500 V	Input DC voltage source
DCin2	500 V	Input DC voltage source
ES	500 V	Energy storage voltage
ESR	18.5 mΩ	Equivalent series resistance of the battery system

Appendix C

This appendix describes the simulation model used in simulation for DDC with LC and LCL filters in Chapter 5.2.2. The software used for circuit simulations is ANSYS Simplorer. An ideal DC voltage source and a resistor act as the load for the DDC. The coupling between the phases is implemented by ideal transformers with 1:1 turns ratio and parallel connected mutual inductances. In the simulations, the duty cycle D was swept through the range [0.1, 0.95] and the coupling coefficient α through the range [-0.05, -0.95]. L_{lk} and L_M were calculated with regard to α and D using equations from Chapter 5.2.1. Table C.1 presents the remaining parameter values used in the simulations.

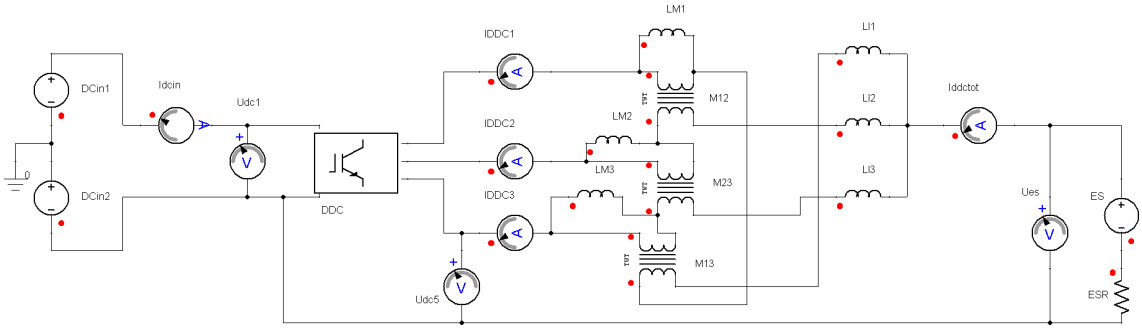

Figure C.1: Simulation model for coupled inductor.

Table C.1: Coupled-inductor simulation model variables.

Variable	Value	Description
DCin1	500 V	Input DC voltage source
DCin2	500 V	Input DC voltage source
Ll1 = Ll2 = Ll3	L_{lk}	Leakage inductance
LM1 = LM2 = LM3	M	Mutual inductance
ES	500 V	Energy storage voltage
ESR	18.5 mΩ	Equivalent series resistance of the battery system